Diversity of the bifurcations and deformations on films bonded to soft substrates: robustness of the herringbone pattern and its cognate patterns

Shotaro Kikuchi[1], *Seishiro Matsubara*[1], *So Nagashima*[1], *Dai Okumura*[1, *]

[1] Department of Mechanical Systems Engineering, Nagoya University, Furo-cho, Chikusa-ku, Nagoya 464-8603, Japan

* Corresponding author.
E-mail address: dai.okumura@mae.nagoya-u.ac.jp (D. Okumura)

ABSTRACT

In this study, we investigate the diversity of the bifurcations and deformations during evolution of periodic patterns on compressed films bonded to compliant substrates. Three-dimensional finite element analysis is performed assuming that the first bifurcation has either the hexagonal or square (i.e., checkerboard) dimple mode. Step-by-step eigenvalue buckling analysis is performed to explore sequential bifurcations on the bifurcated paths. It is found that at the second bifurcation, a rectangular checkerboard or stripe mode occurs depending not only on the Young's modulus ratio of the film and substrate, but also on the magnitude of the imperfection prescribed by the first bifurcation mode. Different bifurcation modes give a family of herringbone deformation patterns with different dimensions, i.e., the evolutional process is multiple and robust. Further, superposition of the identical modes in symmetric directions elucidates the existence of distinctive patterns cognate with the herringbone pattern, including a variety of experimentally observed patterns.

Keywords: Pattern evolution, Surface instability, Buckling, Bifurcation, Elastomers

1. Introduction

Surface instability is one of the classical but challengeable research problems in solid mechanics (Biot, 1963, 1965; Gent and Cho, 1999; Allen, 1969) because most scientists recognize the importance of a basic understanding of evolution and morphogenesis of living systems, such as cortical folding in mammalian brains (Richman et al., 1975; Budday et al., 2014; Tallinen et al., 2014:2016; Kuhl, 2016; Goriely, 2016; Campos et al., 2021). Because brains consist of two layers of gray and white matter, the most elementary model is a compressed film bonded to a compliant substrate (Huang et al., 2005; Kang and Huang, 2010a). The emerging surface patterns gradually evolve as the compressive stress in the film increases beyond a critical buckling stress (Allen, 1969), i.e., as the overstress increases. A small degree of overstress induces hexagonal and square (i.e., checkerboard) dimple patterns (Fig. 1), whereas a large degree of overstress causes the occurrence of herringbone (Fig. 2a) and labyrinth (i.e., disordered herringbone) patterns (Chen and Hutchinson, 2004; Audoly and Boudaoud, 2008a–c; Cai et al., 2011). In contrast, Breid and Crosby (2009, 2011) experimentally observed coexistence of distinctive patterns, such as zipper, peanut, and weave patterns (Fig. 2b,d–f) at large states of overstress, whereas cage-, brick-, and peanut- like patterns have been observed for the intermediate states (Guvendiren et al., 2009). Further, Tallinen and Biggins (2015) found a triple-junction pattern (Fig. 2c), which was energetically comparable with the herringbone pattern. Thus, an open question is: what causes coexistence of diverse and distinctive patterns depending on the degree of overstress?

Chen and Hutchinson (2004) first investigated the occurrence and evolution of herringbone patterns. They performed postbuckling finite element analysis using a small initial imperfection prescribed by the surface deflection of herringbone patterns with different characteristic dimensions, demonstrating that herringbone patterns are dominant at large overstress. They also raised an essential and complicated question, how does the herringbone pattern emerge at large overstress, because the hexagonal and square dimple patterns at small overstress are reproduced by superposing sinusoidal wrinkle modes with a critical wavelength predicted by classical buckling theory (Cai et al., 2011).

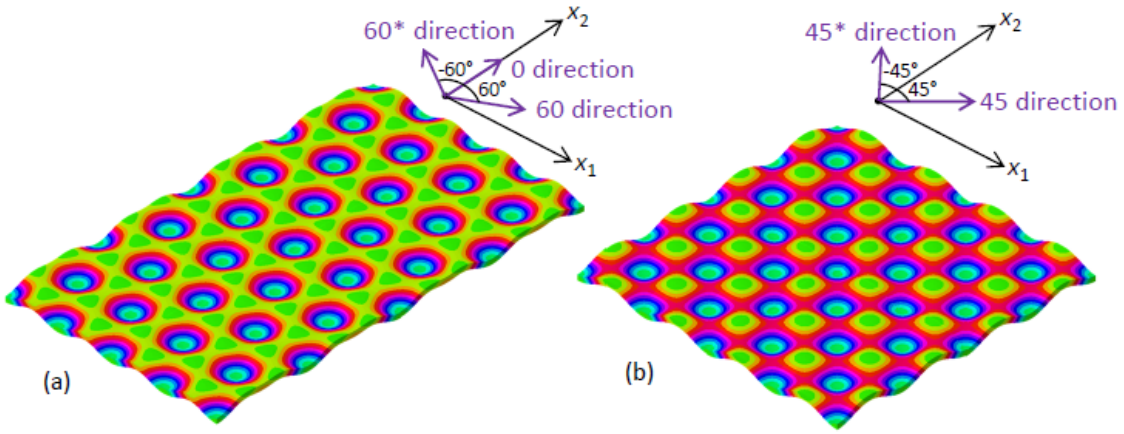

Fig. 1. Surface patterns at small overstress: (a) hexagonal dimple pattern and (b) square dimple (i.e., checkerboard) pattern depicted using 4×4 unit cells (Section 3). These patterns are caused by superposition of sinusoidal wrinkle modes in the symmetric directions assumed at the first bifurcation. The critical bucking stress and wavelength are predicted by classical buckling theory (Allen, 1969). The deformation patterns are essentially the same as the corresponding buckling modes (Fig. 6).

To address the above question, Audoly and Boudaoud (2008a–c) performed linear stability analysis of the straight-stripe buckling mode. They found that second bifurcations lead to the occurrence of undulating-stripe, varicose, checkerboard, and hexagonal buckling modes. The occurrence of the undulating-stripe buckling mode at the second bifurcation can be connected with evolution of a herringbone *deformation pattern* (not a *buckling mode*). They highlighted the great importance of exploring not only the first bifurcation, but also sequential bifurcations occurring on bifurcated paths. Thus, step-by-step eigenvalue buckling and postbuckling analyses (Okumura et al., 2018) were conducted to detect the bifurcation points on the bifurcated paths during evolution of the periodic patterns on a gel film bonded to a soft substrate (Miyoshi et al., 2021). When the hexagonal dimple mode occurred at the first bifurcation, the second bifurcation consisted of rectangular checkerboard modes in three symmetric directions. They revealed that the resulting deformation patterns successfully reproduced the cage- and brick- like patterns at intermediate overstress (Breid and Crosby, 2011), and the third and fourth bifurcations resulted in the occurrence of herringbone patterns.

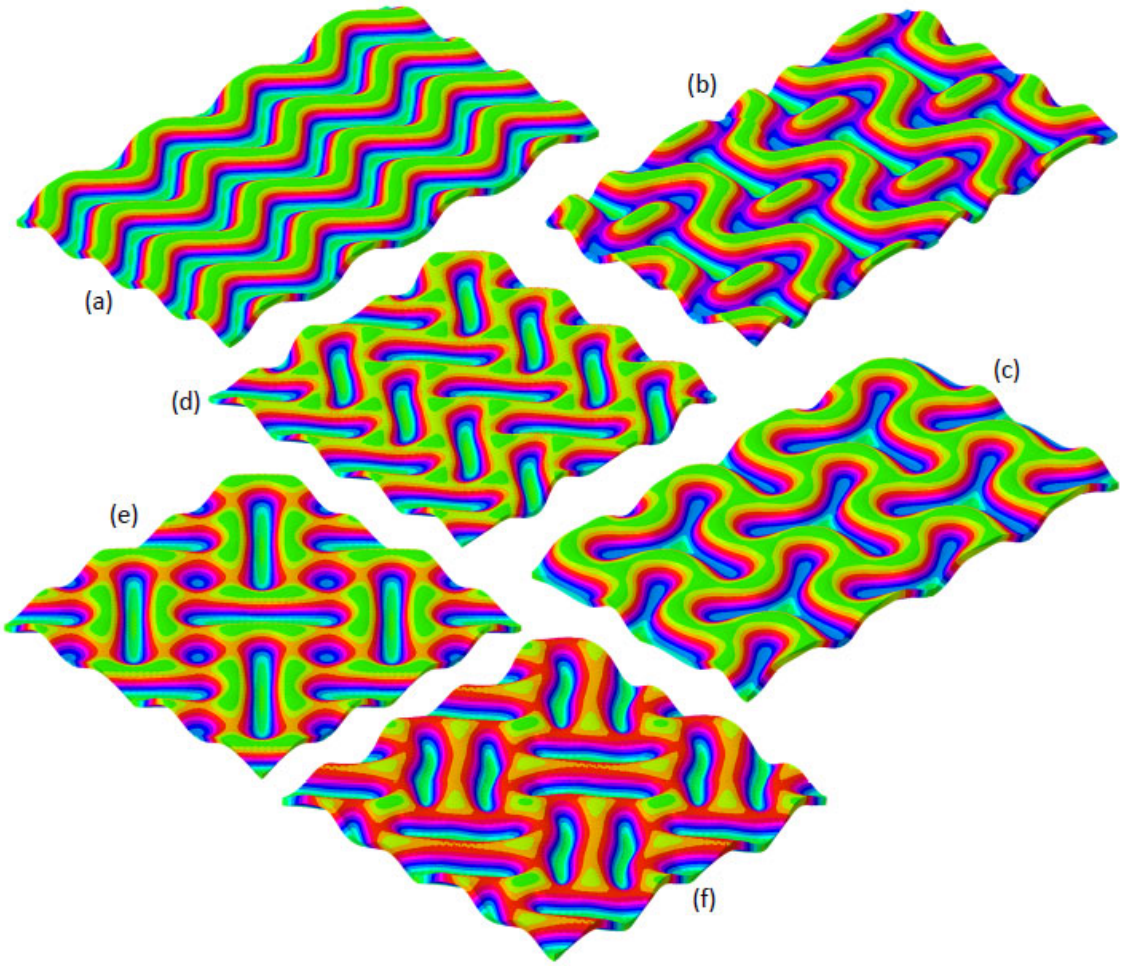

Fig. 2. Diverse and distinctive surface patterns in the range of moderate to large overstress: (a) herringbone pattern, (b) zipper pattern, (c) triple-junction pattern, (d) peanut pattern, (e) plane weave pattern and (f) basket weave pattern depicted using 4×4 unit cells. These images are visualized from the results obtained in the present study (Sections 4–6). The herringbone pattern is well-known to be the representative deformation pattern (not the buckling mode; Chen and Hutchinson, 2004; Miyoshi et al., 2021) at large overstress. In contrast, the zipper, plane weave and peanut patterns have been observed in experiments (Breid and Crosby, 2011; Guvendiren et al., 2009), and the triple-junction pattern has been demonstrated to be energetically comparable with the herringbone pattern by simulations (Tallinen and Biggins, 2015). The question is, what makes these patterns coexist when the overstress increases?

Although the herringbone pattern has been focused on as the representative pattern at large overstress, Tallinen and Biggins (2015) numerically found that the triple-junction pattern can coexist when the film and substrate are of comparable softness. They emphasized that a disordered mixture of herringbone and triple-junction patterns is reminiscent of the folded cerebral cortex, i.e., coexistence of the two patterns

is important for cortical folding. However, the discovery of the triple-junction pattern as the counterpart of the herringbone pattern was heuristic (or intuitive) because their finite element analysis introduced point forces in selected locations of a periodic cell to initiate formation of the patterns. Thus, the mechanisms of the coexistence and the existence of other patterns are still not clear. The approach of Miyoshi et al. (2021) is considered to be a powerful tool for investigating the coexistence of the diverse and distinctive deformation patterns, such as the triple-junction pattern, as well as the experimentally observed zipper and weave patterns (Breid and Crosby, 2011).

In finite element analysis, Miyoshi et al. (2021) considered a specific gel film bonded to a specific soft substrate, i.e., the Flory–Rehner model was used to simulate the inhomogeneous swelling in the gel film (Hong et al., 2009; Kang and Huang, 2010b) and a fixed value of the Young's modulus ratio of the film and substrate was assumed. Further, a fixed magnitude was used as a small scaling factor of the initial imperfection prescribed by the dominant buckling modes needed to trace the corresponding bifurcated path. As suggested by Healey (1989), detection of the second bifurcation can also qualitatively depend on the selected magnitude of the small scaling factor at the first bifurcation. This feature is considered to be an intrinsic problem of the imperfection methods regardless of how the imperfections are prepared (Chen and Hutchinson, 2004; Cai et al., 2011; Tallinen and Biggins, 2015; Miyoshi et al., 2021). However, the approach of Miyoshi et al. (2021) uses superposition of the dominant buckling modes as the initial imperfection so that the value of the imperfection magnitude can be simply parameterized as an additional parameter to investigate the influence. Thus, if the approach of Miyoshi et al. (2021) is extended by parametrizing the two parameters of the Young's modulus ratio and imperfection magnitude, it is expected to obtain more detailed and unified results to understand the mechanisms of the robustness of the herringbone patterns at large overstress and the occurrence of the patterns that can coexist with the herringbone patterns.

In this study, we investigate the diversity of the bifurcations and deformations during evolution of periodic patterns on compressed films bonded to compliant substrates. Section 2 briefly describes the procedures of the eigenvalue buckling and

postbuckling analyses (i.e., step-by-step eigenvalue buckling analysis, Okumura et al., 2018; Miyoshi et al., 2021). The initial imperfections are prepared by superposition of the dominant bifurcation modes obtained on the first and sequential bifurcated paths. Section 3 is devoted to numerical modeling. We focus on both the hexagonal and square dimple modes at the first bifurcation (Fig. 1, Chen and Hutchinson, 2004; Cai et al., 2011) to capture the potential bifurcations and bifurcated paths. Section 4 presents the results obtained from analysis of the second bifurcation point. We find that the second bifurcation has the rectangular checkerboard or stripe mode depending on the Young's modulus ratio of the film and substrate, as well as on the magnitude of the imperfection prescribed by the first bifurcation modes. Further, superposition of the identical bifurcation modes in symmetric directions gives diverse and distinctive modes cognate with the identical mode. Section 5 presents the results of deformation pattern evolution on the second bifurcated path. We find that the herringbone pattern (Fig. 2a) is robust because the different bifurcation modes give a family of herringbone patterns with different characteristic lengths, whereas the occurrence of diverse and distinctive patterns, including the zipper, peanut, weave and triple-junction patterns (Fig. 2b–f), is caused by the modes cognate with the modes leading to the herringbone patterns. Finally, discussion and conclusions are given in Sections 6 and 7, respectively.

2. Procedures of the eigenvalue buckling and postbuckling analyses

This section briefly describes the procedures of the eigenvalue buckling and postbuckling analyses. As explained below, step-by-step eigenvalue buckling analysis is conducted using the BUCKLE option in Abaqus (Abaqus 6.14 User Documentation) to detect the dominant bifurcation point on the bifurcated paths (Okumura et al., 2018; Miyoshi et al., 2021), whereas postbuckling analysis is performed by introducing the corresponding bifurcation modes using the IMPERFECTION option. Although Miyoshi et al. (2021) considered the gel film to obey the Flory–Rehner model to introduce inhomogeneous swelling owing to the increase of the chemical potential (the UHYPER option is needed, Hong et al., 2009), the present study simply considers that both the film and substrate obey the incompressible neo-Hookean solid model. The compressive stress in the film is caused by isotropic thermal expansion. Thus, the increase of the

temperature is used as both a preload and an incremental load in eigenvalue buckling analysis without introducing a dummy loading parameter (Okumura et al., 2018; Miyoshi et al., 2021).

First, for eigenvalue buckling analysis using the BUCKLE option in Abaqus (Abaqus 6.14 User Documentation, 2014; Bertoldi et al., 2008; Miyoshi et al., 2021), the finite element equations are

$$\{\mathbf{K}_0(\mathbf{P})+\lambda_i \mathbf{K}_\Delta(\mathbf{P},\mathbf{Q})\}\boldsymbol{\phi}_i=\mathbf{0} \qquad (i=1, 2, 3,\ldots). \tag{1}$$

Here, $\mathbf{K}_0(\mathbf{P})$ is the stiffness matrix of the base state, where $\mathbf{P}$ is the vector of the nodal forces caused by preloads acting in the base state, while $\mathbf{K}_\Delta(\mathbf{P},\mathbf{Q})$ is the differential stiffness matrix resulting from the incremental loading pattern $\mathbf{Q}$, which is the vector of nodal forces caused by incremental loads added to the base state. Thus, $\mathbf{K}_0(\mathbf{P})$ includes the effects of the geometric and material nonlinearities caused by the preloads (i.e., $\mathbf{P}$) (as well as the influence of bifurcations if the base state is on a bifurcated path), whereas $\mathbf{K}_\Delta(\mathbf{P},\mathbf{Q})$ is obtained by linear perturbation analysis when the incremental loads (i.e., $\mathbf{Q}$) are considered in the base state. Further, λ_i and $\boldsymbol{\phi}_i$ are the eigenvalues (i.e., the multipliers of $\mathbf{Q}$) and the corresponding eigenvectors (i.e., the corresponding buckling modes), where i indicates the i-th buckling mode (i.e., $\lambda_1 \leq \lambda_2 \leq \lambda_3,\ldots$) and $\boldsymbol{\phi}_i$ are normalized such that the maximum displacement component is 1.

Eq. (1) shows that the critical buckling loads are approximately estimated by extrapolation using $\mathbf{Q}$ from the base state prescribed by $\mathbf{P}$ (i.e., $\mathbf{P}+\lambda_i\mathbf{Q}$). Because the dominant bifurcation points are analyzed not only on the primary path, but also on the bifurcated paths, $\mathbf{P}$ is not always zero, and $\mathbf{K}_0(\mathbf{P})$ is not unique depending on the individual bifurcated paths. In other words, the base state is not unique as a function of the magnitude of $\mathbf{P}=r\mathbf{P}_0$. Further, when strong geometric and material nonlinearities appear during λ_i $\mathbf{Q}$, the predictions become less accurate as the value of λ_i increases from 0 to a large value. Thus, step-by-step eigenvalue buckling analysis considers that the dominant bifurcation point is detected by the increase of the magnitude of $\mathbf{P}$, which causes a decrease of the values of λ_i. When at least the minimum eigenvalue, λ_1, is zero, the corresponding magnitude of $\mathbf{P}$ is the critical magnitude of $\mathbf{P}_c=r_c\mathbf{P}_0$ in the critical base state. When multiple bifurcations are assumed as $\lambda_i=0$ (i=1, 2, 3,…, k), Eq. (1)

simply reduces to

$$\mathbf{K}_0(\mathbf{P}_c)\boldsymbol{\phi}_i=\mathbf{0} \qquad \text{when } \lambda_i=0 \ (i=1, 2, 3,\ldots, k), \tag{2}$$

where k is the multiplicity of the bifurcations. Eq. (2) is equivalent to det $\mathbf{K}_0(\mathbf{P}_c)=0$, which is the typical equation used to find the bifurcation points (Hill, 1958; Ohno et al., 2002; Okumura et al., 2004).

The present study considers isotropic thermal expansion to generate the compressive stress in the film bonded to the substrate, i.e., the increase of the temperature is the unique loading parameter that prescribes the preload and incremental load. The critical buckling loads are expressed as $\mathbf{P}(\alpha T)+\Delta T_i\ \mathbf{Q}(\alpha T,\alpha)$, where α is the thermal expansion coefficient, T is the temperature in the base state (i.e., αT is the thermal expansion), and ΔT_i is the incremental temperature from the base state. Eqs. (1) and (2) are rewritten as

$$\{\mathbf{K}_0(\alpha T)+\Delta T_i\ \mathbf{K}_\Delta(\alpha T,\alpha)\}\boldsymbol{\phi}_i=\mathbf{0} \qquad (i=1, 2, 3,\ldots), \tag{3}$$

$$\mathbf{K}_0(\alpha T_c)\boldsymbol{\phi}_i=\mathbf{0} \qquad \text{when } \Delta T_i=0 \ (i=1, 2, 3,\ldots, k). \tag{4}$$

Although Eq. (3) shows that $T+\Delta T_i$ are the critical buckling temperatures, Eq. (4) shows that the dominant bifurcation point is accurately estimated by the critical value of T_c with $\Delta T_i=0$ ($i=1, 2, 3,\ldots, k$). Note that although the two values of $T+\Delta T_i$ ($i=1, 2, 3,\ldots, k$) and T_c may be close, the corresponding buckling modes are not necessarily the same. To decrease the lowest eigenvalue (ΔT_1) to 0, Eq. (3) is analyzed using individual base states by the step-by-step increase of T. The base state with $\Delta T_1=0$ (in reality, it approximates zero) is regarded as the dominant bifurcation point described by Eq. (4), i.e., if ΔT_1 remains positive ($\Delta T_1>0$), the base state is stable whereas if not, that is unstable. The multiplicity of bifurcations (k) is estimated by comparing ΔT_i ($i=2, 3, 4,\ldots$) with ΔT_1 at the critical base state. Because multiple bifurcations cause loss of symmetry of the base state, the value of k can also be determined by checking the bifurcation modes $\boldsymbol{\phi}_i$ ($i=1, 2, 3,\ldots, k$). The dominant bifurcation point on the bifurcated paths is analyzed by repeating postbuckling analysis to trace the corresponding bifurcated path (Fig. 3).

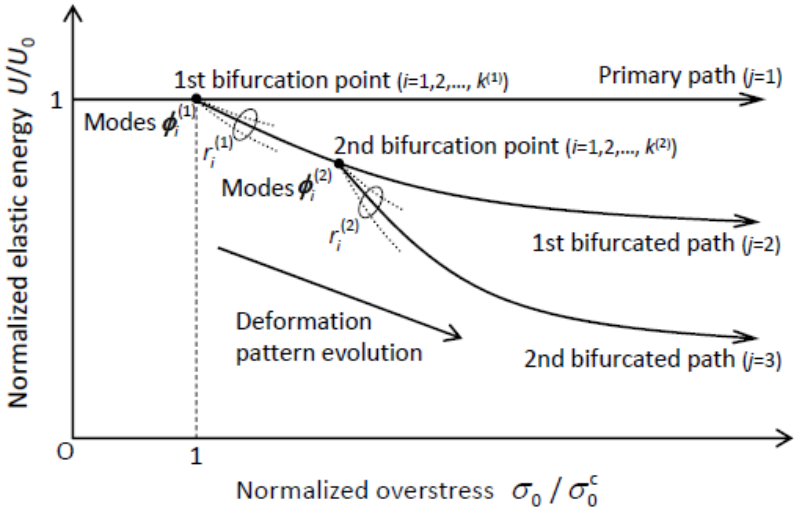

Fig. 3. Schematic illustration of pattern evolution caused by multiple and sequential bifurcations. Evolution of the deformation patterns leads to relative decreases of the normalized elastic energy (U/U_0) as the normalized overstress (σ_0 / σ_0^c) increases (Section 3.3). The dominant bifurcation points on the primary and bifurcated paths are detected by step-by-step eigenvalue buckling analysis (Eqs. (3) and (4)), and pattern evolution is traced by postbuckling analysis using the bifurcation modes as imperfections. The imperfection magnitude ($d^{(1)}$, Eq. (6)) is parameterized because the second and sequential bifurcation points depend on the value (Section 4).

Postbuckling analysis is performed by introducing the dominant bifurcation modes as a geometric imperfection (the IMPERFECTION option in Abaqus). When multiple bifurcations are considered (Eq. (4)), the imperfection ($\Delta\boldsymbol{\phi}$) introduced as initial geometric imperfections is expressed as

$$\Delta\boldsymbol{\phi} = d\sum_{i=1}^{k} r_i\boldsymbol{\phi}_i \,, \tag{5}$$

where d is an imperfection magnitude and r_i are the coefficients that control and normalize the contributions of $\boldsymbol{\phi}_i$ (i=1, 2, 3,…, k). The present study focuses on analysis of the nth bifurcation on the (n−1)th bifurcated path (see Fig. 3, the 0-th bifurcated path is the primary path). When $d^{(j)}$, $k^{(j)}$, $r_i^{(j)}$, and $\boldsymbol{\phi}_i^{(j)}$ (i=1, 2, 3,…, $k^{(j)}$) are assigned as the extended values of d, k, r_i, and $\boldsymbol{\phi}_i$ (i=1, 2, 3,…, k) for the jth bifurcation point on the (j−1)th bifurcated path, the initial geometric imperfections needed to trace the nth bifurcated path are

$$\Delta\boldsymbol{\phi}^{(n)} = \sum_{j=1}^{n}\left(d^{(j)}\sum_{i=1}^{k^{(j)}} r_i^{(j)}\boldsymbol{\phi}_i^{(j)} \right). \tag{6}$$

The bifurcations and deformations during pattern evolution are investigated by

repeating the eigenvalue buckling and postbuckling analyses on the bifurcated paths (Fig. 3). Hence, the dominant bifurcation point detected on a bifurcated path estimates a base state to be stable before the point and unstable after the point.

According to Healey (1989), imperfection methods, including the present approach (Eq. (6)), can fail to trace the bifurcated path related to the corresponding buckling mode. The justification of the bifurcated path should be confirmed by comparing pattern evolution in postbuckling with the imperfection generated by Eq. (6). Although as shown and described in Sections 4–6, most of the bifurcated paths did not cause accidental path switching, this feature is considered to be an intrinsic problem of imperfection methods. In contrast, this feature raises an open and interesting question: does the dominant bifurcation mode at the second bifurcation (or the jth bifurcation) depend on the imperfection magnitudes, $d^{(1)}$ (and $d^{(l)}$, l=1,2,…, j–1), used to trace the first bifurcated path (and the (l–1)th bifurcated paths, l=2,3,…, j–1)? To address this question, in the present study, we analyze the second bifurcation by considering the imperfection magnitude of $d^{(1)}$ as an additional parameter (Section 4).

3. Numerical modeling

3.1. Material properties

To reproduce compressed films bonded to compliant substrates, both of the film and substrate are considered to obey the incompressible neo-Hookean solid model, i.e., the substrate is modeled using the Young's modulus E_s, whereas the film is modeled using the Young's modulus E_f and isotropic thermal expansion α. An increase of the temperature T causes an increase of the in-plane compressive stresses in the film, which are equibiaxial at least on the primary path. The ratio of the Young's moduli (E_f/E_s) is parameterized in the range 2–20 (Breid and Crosby, 2011; Tallinen and Biggins, 2015; Campos et al., 2021).

3.2. Boundary conditions

Fig. 4 shows the periodic cells used in three-dimensional (3D) finite element analysis, which are commonly defined as rectangular parallelepiped with individual lengths of L_1, L_2, h, and H. The lengths normalized using h (i.e., L_1/h, L_2/h, and H/h) are

specified in Section 3.4. The film is perfectly bonded on the substrate (x_3=H). The bottom face of the substrate (x_3=0) has zero displacement, i.e., u_i (x_1, x_2, 0)=0, while the top face of the film (x_3=h+H) is stress free. Periodic boundary conditions are imposed on the side faces (the combination of x_1=(0 or L_1) or x_2=(0 or L_2)), and they are expressed as

$$\begin{cases} u_i(0,x_2,x_3) = u_i(L_1,x_2,x_3) \\ u_i(x_1,0,x_3) = u_i(x_1,L_2,x_3) \end{cases}, \tag{7}$$

where u_i(x_1, x_2, x_3) is the displacement at a nodal point. From the repulsive forces acting on the side faces, the in-plane components of the macroscopic nominal stress (S_{11} and S_{22}) can be calculated (Miyoshi et al., 2021).

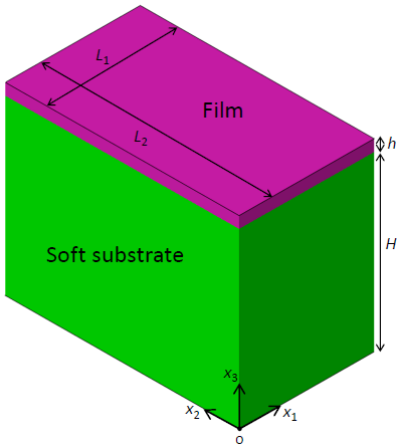

Fig. 4. Initial dimensions of the compressed films bonded to soft substrates. The individual lengths are normalized with respect to h (i.e., L_1/h, L_2/h, and H/h). The value of H/h is selected to be sufficiently large to avoid having to consider the effects of the constraint at the bottom face (Huang et al., 2005). The compressive stress is given by the isotropic thermal expansion in the film and the increase of the temperature.

3.3. Normalization of the overstress and elastic energy

Although calculation of S_{11} and S_{22} is convenient to estimate the critical values on bifurcated paths, the present study simply uses the concept of the overstress (Chen and Hutchinson, 2004; Cai et al., 2011). The overstress ($\sigma_0(T)$) is a function of T, and it is defined as the homogenous stress in the film on the primary path. When the first bifurcation has the critical value $\sigma_0^c(T_1)$ (T_1 is the critical temperature for the first bifurcation), the critical values of the temperature for sequential bifurcations (T_i, i=2, 3,…) are transformed and estimated as the critical ratios of the corresponding overstress,

i.e., $\sigma_0(T_i)/\sigma_0^c(T_1)$. Thus, $\sigma_0(T_i)/\sigma_0^c(T_1)$ =1 at the first bifurcation and it monotonically increases, which is used to estimate the sequential bifurcation points and bifurcated paths. In the same manner, the elastic energy per unit area of the film/substrate system is defined as $U(T)$ as a function of temperature T. This value can be calculated regardless of the primary and bifurcated paths. Thus, the normalized elastic energy per unit volume is estimated by $U(T)/U_0(T)$, where $U_0(T)$ is the elastic energy per unit volume on the primary path. $U(T)/U_0(T)$=1 on the primary path and decreases with the occurrence of bifurcations. To avoid redundancy, $\sigma_0(T_i)/\sigma_0^c(T_1)$ and $U(T)/U_0(T)$ are expressed as σ_0/σ_0^c and U/U_0, respectively. The occurrence of bifurcations causes a decrease of U/U_0 with an increase of σ_0/σ_0^c (Fig. 3). Hereafter, because there is no reason to consider a specific value of α, we arbitrarily set α =0.01 and do not show and discuss the individual values of T.

3.4. Dimensions of the unit and periodic cells

The present study considers the occurrence of hexagonal and square (i.e., checkerboard) dimple modes (Fig. 1) at the first bifurcation point on the primary path (Chen and Hutchinson, 2004; Cai et al., 2011). Because the first bifurcation consists of superposing sinusoidal wrinkle modes in all directions in the plane with a critical wavelength (Allen, 1969), a specific ratio of L_2/L_1 is used to give the hexagonal or square dimple mode as the dominant bifurcation mode. According to the appendix B in Miyoshi et al. (2021), the specific value of $L_2/L_1=\sqrt{3}$ generates the hexagonal dimple mode consisting of the combination of the sinusoidal wrinkle modes categorized by (m, n)=(0, 2) and (m, n)=(1, 1), where m and n are the wavenumbers in the x_1 and x_2 directions. The angles between the individual wave directions are $60°$ (Fig. 1a) and the wavelength is $\lambda=0.5L_2$. In contrast, the square dimple mode is obtained by using L_2/L_1=1 and the present study considers the combination of the sinusoidal wrinkle modes categorized by (m, n)=(1, 1). Thus, the angles between the two wave directions are $45°+45°=90°$ (Fig. 1b) and the wavelength is $\lambda=0.71(\approx 1/\sqrt{2})L_2$. Note that the set of ($m$, n)=(1, 0) and (m, n)=(0, 1) can be used to give the square dimple mode with $\lambda=L_2(=L_1)$ but using (m, n)=(1, 1) facilitates comparison of the hexagonal and square dimple modes because the number of dimples are the same in the unit cells (Fig. 1).

Because the ratio of L_2/L_1 is fixed to consider the hexagonal or square dimple mode, the critical value of L_{2c}/h is detected by finding $\sigma_0^c(T_1)$ as the minimum value among the values calculated by changing the value of L_2/h (Miyoshi et al., 2021). Thus, the critical wavelength is expressed as $\lambda_c/h=0.5L_{2c}/h$ for the hexagonal dimple mode and $\lambda_c/h=0.71L_{2c}/h$ for the square dimple mode (see Appendix A).

Fig. 5 shows the unit cells and finite element meshes used to detect L_{2c}/h. 3D finite element analysis is performed using the eight-node linear brick element with the element type C3D8RH. The numbers of nodes and elements are 31,226 and 28,800 for $L_2/L_1=\sqrt{3}$, and 24,986 and 22,500 for $L_2/L_1=1$, respectively. The same meshes are used for different values of L_2/h. The value of $H/h=95$ is selected to be sufficiently large to avoid having to consider the effects of the constraint at the bottom face (Huang et al., 2005). Note that to visualize the finite element meshes of the film, Fig. 5 does not show the entire length of H/h. The mesh resolution and H/h value were determined by trial-and-error analysis to decrease computational cost. The element type C3D8RH falls into first-order, reduced-integration elements. Thus, hourglass control is enhanced in Abaqus analysis, resulting in yielding artificial strain energy associated with the constraints used to remove singular modes. The present study estimates the value of U/U_0 by removing this artificial contribution from the total strain energy in the system (i.e., the ALLSE identifier is used in Abaqus). The artificial contribution was confirmed to be negligible (less than 4%) of the total strain energy and have no qualitative influence on the results in Sections 4–6.

When the critical values of L_{2c}/h for $L_2/L_1=1$ and $\sqrt{3}$ are detected depending on the value of E_f/E_s (Appendix A), the large periodic cell consisting of 2×2 unit cells (not the 1×1 unit cells in Fig. 5) is analyzed to investigate the evolution of the periodic pattern from the hexagonal and square dimple modes. If necessary, 4×4 unit cells are also assumed (Appendix B). These periodic cells are referred to as 2×2 and 4×4 unit cells to distinguish them from the 1×1 unit cell. Each unit cell is discretized using the same finite element meshes as the unit cell (Fig. 5). The present study mainly uses the 2×2 unit cell. This restriction on periodic cells was considered to avoid a tremendous increase of computational cost. Note that the possibility of the occurrence of longer

wavelength bifurcations (Geymonat et al., 1993; Okumura et al., 2004; Ohno et al., 2004) is excluded in the present study.

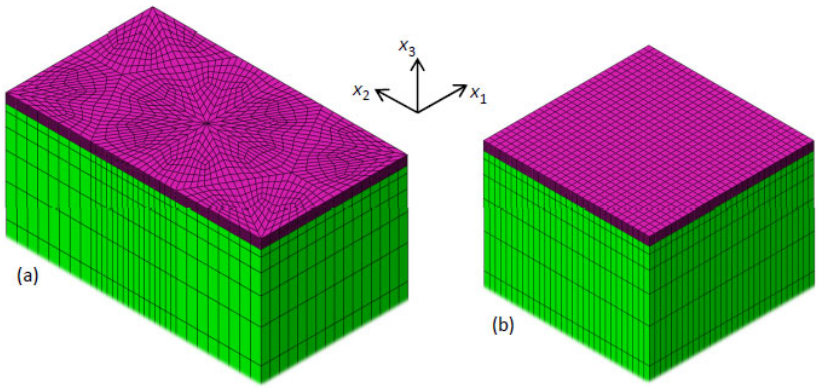

Fig. 5. Finite element meshes of the unit cells for the (a) hexagonal dimple mode with $L_2/L_1=\sqrt{3}$ and (b) square dimple mode with $L_2/L_1=1$. Different values of L_2/h are considered to detect the dominant wavelength, which depends on the Young's modulus ratio, E_f/E_s. The trial-and-error analysis determined the use of $H/h=95$ as an approximation of $H/h\to\infty$. Note that to visualize the finite element meshes of the film, the figures do not include the entire length of H/h. The unit cells are called the 1×1 unit cell to distinguish them from the periodic cells consisting of $n\times n$ unit cells.

The expression $\{L_2/L_1, E_f/E_s, d^{(1)}/h\}$ is used to indicate the parameter set used in the analysis, i.e., $L_2/L_1=\sqrt{3}$ for the hexagonal dimple mode and $L_2/L_1=1$ for the square dimple mode, E_f/E_s is parameterized as the Young's modulus ratio, and $d^{(1)}/h$ is parameterized as the imperfection magnitude introduced at the first bifurcation to trace the first bifurcated path (Eq. (6)).

Fig. 6 shows the responses of the first bifurcated paths obtained using the 2×2 unit cell. The parameter sets of $\{L_2/L_1, E_f/E_s, d^{(1)}/h\}=\{\sqrt{3}$ or 1, 15, 0.01$\}$ were used as an example. The critical wavelength is $\lambda_c/h=12.4$ (Appendix A). An increase of σ_0/σ_0^c from 1 causes a decrease of U/U_0 from 1 (Fig. 6a), i.e., pattern evolution occurs. The hexagonal and square dimple modes ($\boldsymbol{\phi}_{HEX}^{(1)}$ and $\boldsymbol{\phi}_{SQU}^{(1)}$) at the first bifurcation (Fig. 6b,d) lead to evolution of the deformation patterns on the first bifurcated path (Fig. 6c,e). The bifurcation modes just correspond to the deformation patterns on the first bifurcated path (Fig. 6b–e). As described by Cai et al. (2011), the square dimple (i.e., checkerboard) pattern is superior to the hexagonal dimple pattern (Fig. 6a). However,

the energy difference is very small and can be considered to be negligible in the case where the film and substrate are assumed to be incompressible (Section 3.1) with a small Young's modulus ratio in the range 2–20 (cf. Chen and Hutchinson, 2004; Cai et al., 2011). Thus, both the hexagonal and square dimple patterns are considered to investigate the pattern evolutions on the second and sequential bifurcated paths (Sections 4–6). In addition, the second bifurcation points are detected at small overstresses of $\sigma_0 / \sigma_0^c < 1.8$.

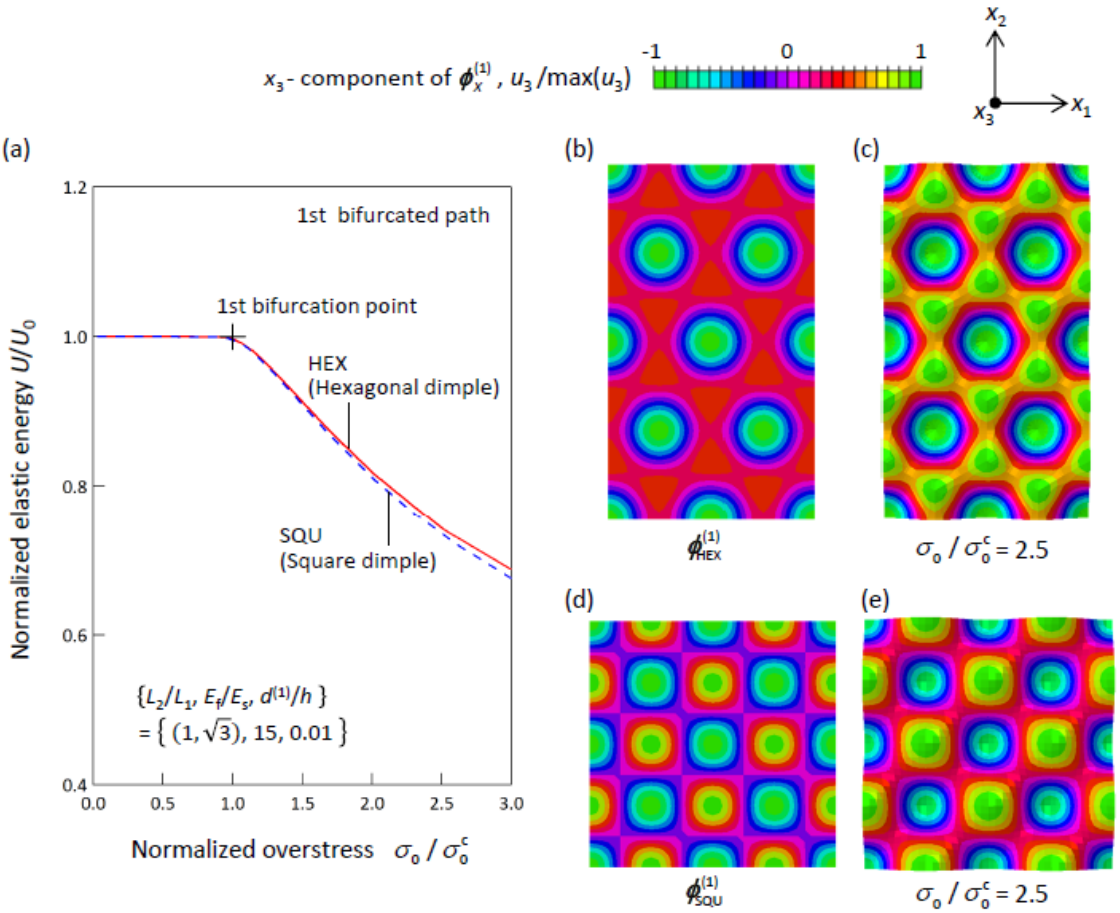

Fig. 6. Responses of the first bifurcated paths obtained using the 2×2 unit cell with $\{L_2/L_1, E_f/E_s, d^{(1)}/h\}=\{(1,\sqrt{3}), 15, 0.01\}$ as an example. (a) U/U_0 as a function of σ_0 / σ_0^c, (b) $\phi_{HEX}^{(1)}$, (c) the hexagonal dimple pattern induced by $\phi_{HEX}^{(1)}$, (d) $\phi_{SQU}^{(1)}$, and (e) the square dimple pattern induced by $\phi_{SQU}^{(1)}$. It is clear that the bifurcation modes correspond to the deformation patterns on the first bifurcated path. The energy difference between the two patterns is very small and can be considered to be negligible because the present study assumes that the film and substrate are incompressible with a small Young's modulus ratio in the range 2 – 20 (cf. Cai et al., 2011).

4. Results from analysis of the second bifurcation point

4.1. Bifurcation modes at the second bifurcations

Fig. 7 shows the second bifurcation points on the first bifurcated paths. Using $\{L_2/L_1, E_f/E_s, d^{(1)}/h\}=\{(1,\sqrt{3}), (3,6,20), 0.01\}$ (Fig. 7a), the effects of L_2/L_1 and E_f/E_s on the first bifurcated path are almost invisible, especially in the range $\sigma_0/\sigma_0^c < 2$. Similarly, using $\{L_2/L_1, E_f/E_s, d^{(1)}/h\}=\{\sqrt{3}, 9, (0.001, 0.05, 0.1)\}$ (Fig. 7b), the energy difference is hardly visible, except for the case of $d^{(1)}/h=0.1$ (i.e., this is the largest value of the imperfection magnitude). However, appearance of the second bifurcation points in the early stage of overstress ($\sigma_0/\sigma_0^c=1$–1.8) strongly depends on the variation of these parameter sets. The hexagonal dimple pattern ($L_2/L_1=\sqrt{3}$) has four types of second bifurcations, whereas the square dimple pattern ($L_2/L_1=1$) has three types. The bifurcation modes are different (Figs. 8 and 9), which are categorized as Fields HA, HB, HC, and HD for the hexagonal dimple pattern (Fig. 10) and Fields SA, SB, and SC for the square dimple pattern (Fig. 11). The second bifurcation modes are detected as a function of not only E_f/E_s (Fig. 7a), but also $d^{(1)}/h$ (Fig. 7b).

Fig. 8 shows the second bifurcation modes occurring during evolution of the hexagonal dimple pattern. The second bifurcation included in Field HA has $k^{(2)}=2$ (i.e., it is a double bifurcation). Fig. 8a,b shows the two basic bifurcation modes, $\boldsymbol{\phi}_{\mathrm{HA0a}}^{(2)}$ and $\boldsymbol{\phi}_{\mathrm{HA0b}}^{(2)}$, which are recognized as an identical rectangular checkerboard mode with translational symmetry in the x_2 direction. In contrast, Fields HB and HC have $k^{(2)}=3$ (i.e., they are triplet bifurcations). The basic bifurcation modes of Field HB ($\boldsymbol{\phi}_{\mathrm{HB0}}^{(2)}$, $\boldsymbol{\phi}_{\mathrm{HB60}}^{(2)}$, and $\boldsymbol{\phi}_{\mathrm{HB60*}}^{(2)}$, Fig. 8c–e) are an identical stripe mode occurring in three symmetric directions because of the hexagonal dimple pattern (Fig. 1a), whereas the bifurcation modes of Field HC ($\boldsymbol{\phi}_{\mathrm{HC0}}^{(2)}$, $\boldsymbol{\phi}_{\mathrm{HC60}}^{(2)}$, and $\boldsymbol{\phi}_{\mathrm{HC60*}}^{(2)}$, Fig. 8f–h) are an identical rectangular checkerboard mode occurring in the symmetric directions. Although Miyoshi et al. (2021) discovered the importance of $\boldsymbol{\phi}_{\mathrm{HC0}}^{(2)}$, $\boldsymbol{\phi}_{\mathrm{HC60}}^{(2)}$, and $\boldsymbol{\phi}_{\mathrm{HC60*}}^{(2)}$ as the second bifurcation modes for surface pattern evolution of a gel film bonded to a substrate, the present study elucidates that the second bifurcations detected during evolution of the hexagonal dimple pattern are not unique and the sets of the dominant bifurcation modes are categorized in Fields HA, HB, HC, and HD (Fig. 10).

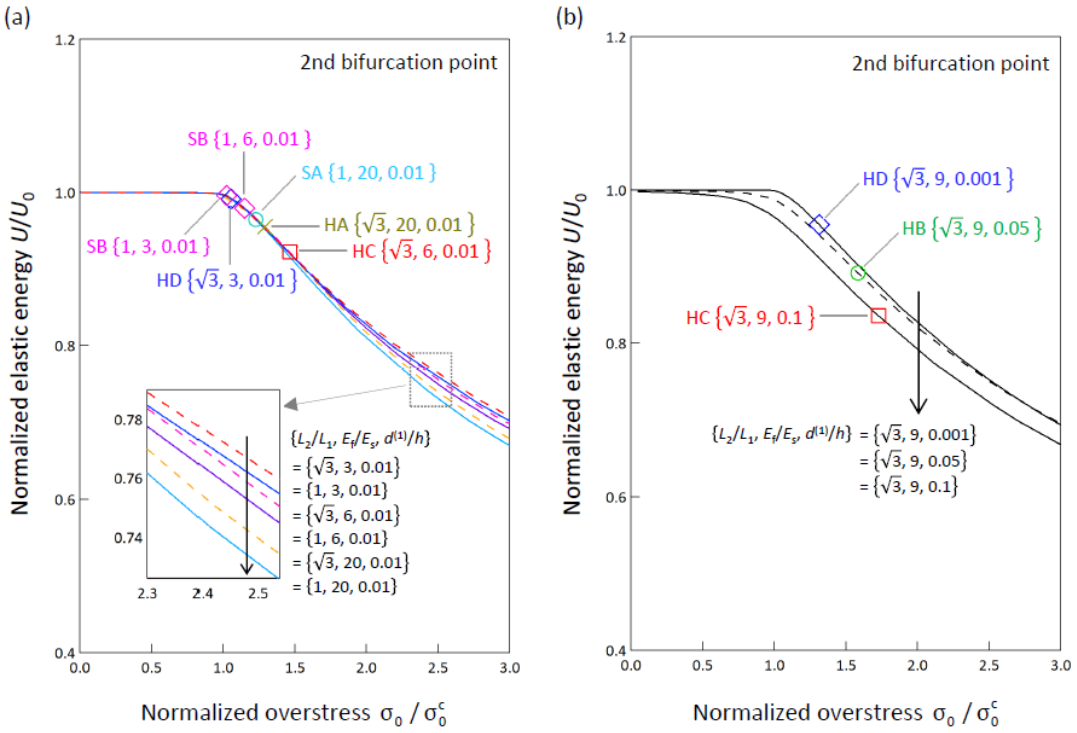

Fig. 7. Second bifurcation points on the first bifurcated paths using the parameter sets of (a) $\{L_2/L_1,\ E_f/E_s,\ d^{(1)}/h\}=\{(1,\sqrt{3}),\ (3,6,20),\ 0.01\}$ and (b) $\{L_2/L_1,\ E_f/E_s,\ d^{(1)}/h\}=\{\sqrt{3},\ 9,\ (0.001,\ 0.05,\ 0.1)\}$. The present study analyzes the second bifurcation point on the first bifurcated path for individual parameter sets. The hexagonal dimple pattern ($L_2/L_1=\sqrt{3}$) has four types of second bifurcations, which consist of different sets of bifurcation modes (Fig. 8), and belong to Fields HA, HB, HC, and HD (Fig. 10), whereas the square dimple pattern ($L_2/L_1=1$) has three types of second bifurcations, which also consist of different sets of bifurcation modes (Fig. 9), and belong to Fields SA, SB, and SC (Fig. 11). Thus, the bifurcation modes are detected as a function of not only E_f/E_s, but also $d^{(1)}/h$ in the early stages of overstress ($\sigma_0 / \sigma_0^c=1$–1.8).

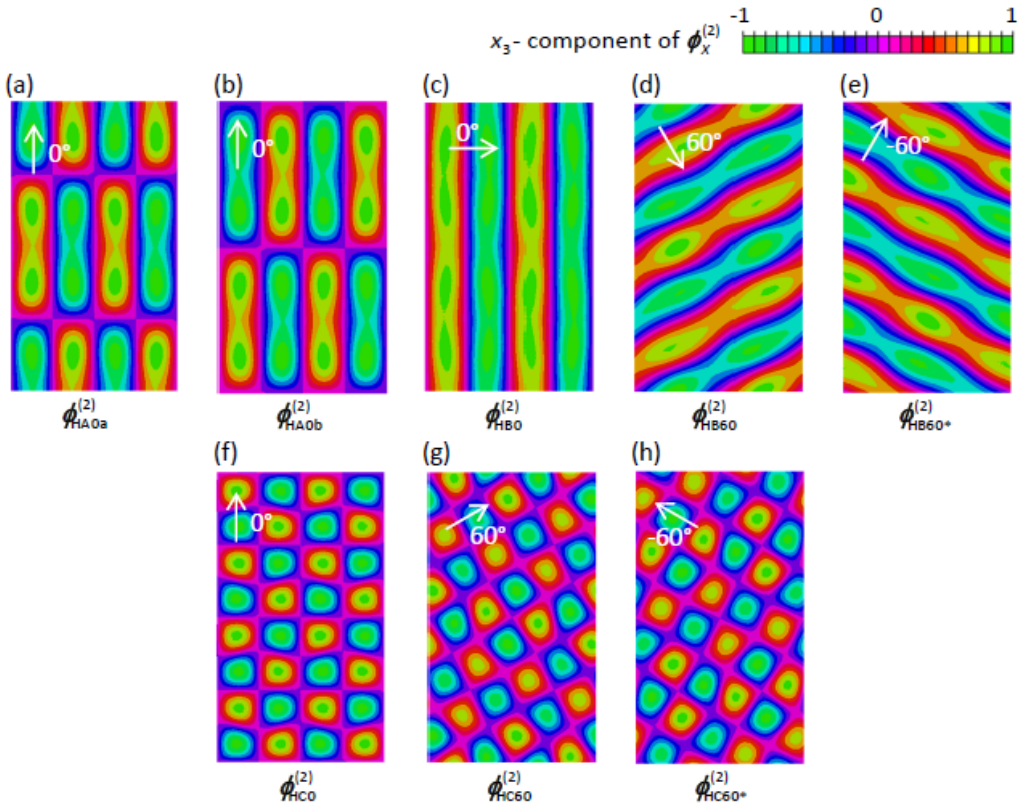

Fig. 8. Bifurcation modes at the second bifurcation occurring during evolution of the hexagonal dimple pattern analyzed using the parameter sets of $\{L_2/L_1, E_f/E_s, d^{(1)}/h\}$. (a) and (b) $\phi_{HA0a,b}^{(2)}$ for $\{\sqrt{3}, 20, 0.01\}$ ($k^{(2)}$=2), (c)–(e) $\phi_{HB0,60,60*}^{(2)}$ for $\{\sqrt{3}, 9, 0.01\}$ ($k^{(2)}$=3), and (f)–(h) $\phi_{HC0,60,60*}^{(2)}$ for $\{\sqrt{3}, 6, 0.01\}$ ($k^{(2)}$=3). The subscripts HA, HB, and HC indicate that the bifurcation modes represent the modes obtained in Fields HA, HB, and HC, respectively (Fig. 10). Modes $\phi_{HC0,60,60*}^{(2)}$ are the rectangular checkerboard modes in the three symmetric directions reported by Miyoshi et al. (2021). Modes $\phi_{HA0a,b}^{(2)}$ are the same rectangular checkerboard mode with a phase shift in the x_2 direction because of the translational symmetry. In contrast, Modes $\phi_{HB0,60,60*}^{(2)}$ are the stripe modes in the three symmetric directions.

The second bifurcation modes occurring during evolution of the square dimple pattern are shown in Fig. 9. Fields SA and SB have $k^{(2)}$=4 and $k^{(2)}$=2, respectively, so Fig. 9a–d show $\phi_{SA0a}^{(2)}$, $\phi_{SA0b}^{(2)}$, $\phi_{SA90a}^{(2)}$, and $\phi_{SA90b}^{(2)}$ for Field SA, whereas Fig. 9e,f show $\phi_{SB45}^{(2)}$ and $\phi_{SB45*}^{(2)}$ for Field SB. For Field SA, $k^{(2)}$=4 results from the identical rectangular checkerboard modes extended by the rotational symmetry between the x_1 and x_2 directions and the translational symmetry in the x_1 or x_2 direction. For Field SB, $k^{(2)}$=2 means the identical rectangular checkerboard mode in the ±45° directions to the x_1 or x_2 direction (Fig. 1b). It is interesting that Fields HA, HC, SA and SB consist of a series of analogous rectangular checkerboard modes and only Field HB consists of the stripe modes (Figs. 8 and 9). Fields HA, HB, HC, HD, SA, SB, and SC are found by

parameterizing not only E_f/E_s but also $d^{(1)}/h$. The bifurcation modes in Fields HD and SC are not shown here. The reason for this will be given in Section 4.2.

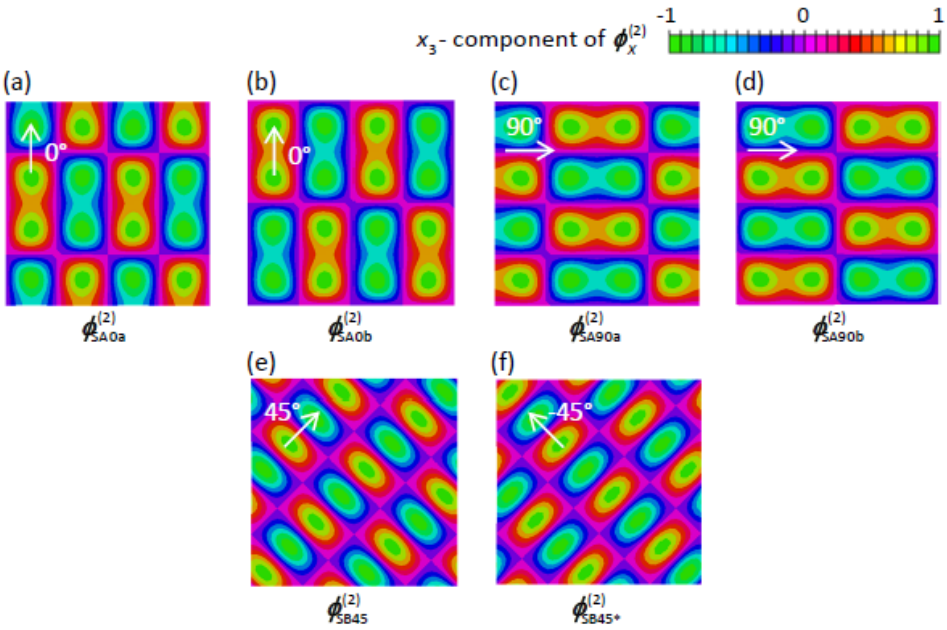

Fig. 9. Bifurcation modes at the second bifurcation occurring during evolution of the square dimple pattern analyzed using the parameter sets of $\{L_2/L_1, E_f/E_s, d^{(1)}/h\}$. (a)–(d) $\phi_{SA0a,b,90a,b}^{(2)}$ for $\{1, 15, 0.01\}$ ($k^{(2)}$=4), and (e) and (f) $\phi_{SB45,45*}^{(2)}$ for $\{1, 5, 0.01\}$ ($k^{(2)}$=2). The subscripts SA and SB indicate that the bifurcation modes represent the modes obtained in Fields SA and SB (Fig. 11). They belong to the rectangular checkerboard modes. Multiplicity of the bifurcations occurs owing to the translational and/or rotational symmetries.

4.2. Bifurcation mode diagrams of the second bifurcation

As shown in Section 4.1, the dominant bifurcation modes depend on not only E_f/E_s, but also $d^{(1)}/h$. To elucidate the interactions between the two parameters, Figs. 10 and 11 show that the bifurcation mode diagrams of the second bifurcation occurring during the evolution of the hexagonal and square dimple patterns, respectively. First, the bifurcation mode diagrams are depicted as a function of E_f/E_s and the value of σ_0/σ_0^c detected at the second bifurcation point (i.e., $\sigma_0^{(2)}/\sigma_0^c$) (Figs. 10a and 11a). In these graphs, the points obtained by the same value of $d^{(1)}/h$ are connected by individual lines. The value of $d^{(1)}/h$ affects not only the value of $\sigma_0^{(2)}/\sigma_0^c$, but also the dominant bifurcation mode. Thus, if imperfection methods are used such as in the present study (Section 2), a fixed value of the imperfection magnitude can fail to obtain the comprehensive responses that depend on the imperfection magnitude in analysis of the

second and sequential bifurcations. This leads to the need to show the bifurcation mode diagram as a function of not only E_f/E_s, but also $d^{(1)}/h$. (Figs. 10b and 11b). Figs. 10 and 11 clearly demonstrate the existence of Fields HA, HB, HC, and HD for the hexagonal dimple pattern and Fields SA, SB, and SC for the square dimple pattern. The individual fields are confirmed to include the parameter sets of the specific values used to show Figs. 8 and 9.

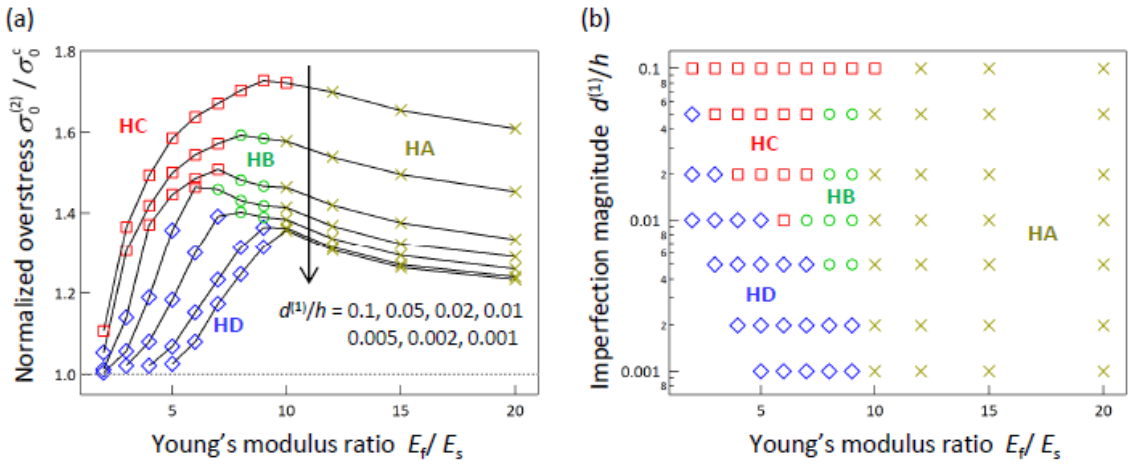

Fig. 10. Bifurcation mode diagrams of the second bifurcation occurring during evolution of the hexagonal dimple pattern as a function of (a) E_f/E_s and $\sigma_0^{(2)}/\sigma_0^c$ and (b) E_f/E_s and $d^{(1)}/h$. The diagrams show Fields HA, HB, and HC in which the bifurcation modes are $\phi^{(2)}_{HA0a,b}$, $\phi^{(2)}_{HB0,60,60*}$ and $\phi^{(2)}_{HC0,60,60*}$, respectively (Fig. 8). The bifurcation modes belong to either Field HA, HB, HC, or HD. Field HD consists of a subset of the sinusoidal wrinkle modes at the first bifurcation, so the present study considers Field HD to be a meaningless field.

Note that the present study considers Fields HD and SC to be meaningless fields of the second bifurcation because the bifurcation modes are a subset of the sinusoidal wrinkle modes obtained at the first bifurcation, i.e., the parameter sets distributed in the two fields (Figs. 10 and 11) fail to detect the second bifurcation. This tendency is reasonably understood by the first bifurcation point being multiple ($k^{(1)}\neq1$) and the potential bifurcation modes, except for the hexagonal and square dimple modes still being available at low overstress (i.e., at $\sigma_0^{(2)}/\sigma_0^c$=1–1.4 in Figs 10a and 11a). Because Fields HD and SC also depend on the value of E_f/E_s, the imperfection magnitude should be parameterized to recognize and avoid the fields. For instance, using $d^{(1)}/h$=0.01 (a popular value used in imperfection methods, Chen and Hutchinson, 2004; Cai et al., 2011; Miyoshi et al., 2021) fails to detect the second bifurcation point when the value of

E_f/E_s is smaller than 5 for the hexagonal dimple pattern. Perfect nonlinear bifurcation analysis (not imperfection methods, e.g., Healey, 1988; Ohno et al., 2002; Okumura et al., 2004; Pandurangi et al., 2020) solves this intrinsic problem, but, unfortunately, the finite element packages, including Abaqus, do not have this option (Healey, 1989).

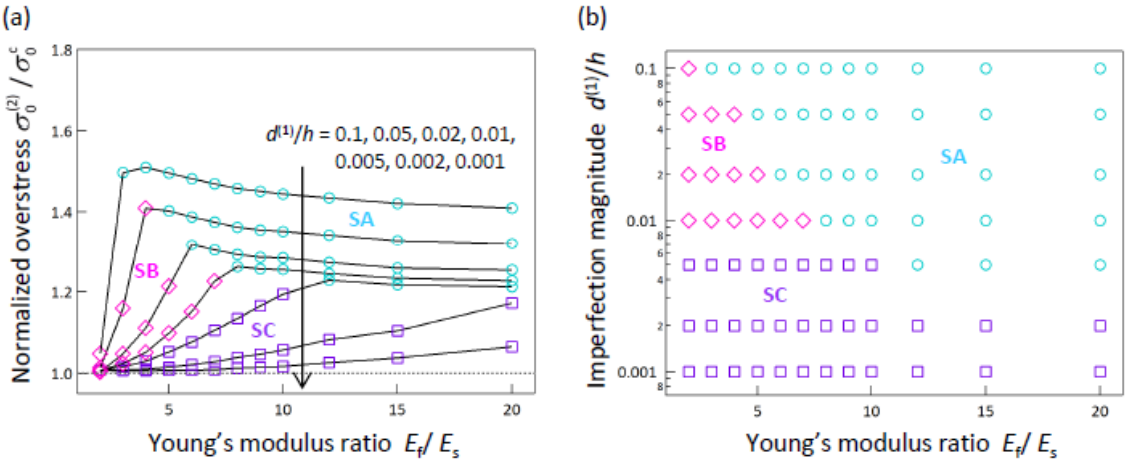

Fig. 11. Bifurcation mode diagrams of the second bifurcation occurring during evolution of the square dimple pattern as a function of (a) E_f/E_s and $\sigma_0^{(2)}/\sigma_0^c$ and (b) E_f/E_s and $d^{(1)}/h$. The diagrams show Fields SA and SB in which the bifurcation modes are $\boldsymbol{\phi}^{(2)}_{SA0,90}$ and $\boldsymbol{\phi}^{(2)}_{SB45,45*}$ (Fig. 9). The bifurcation modes belong to either Field SA, SB, or SC. Field SC consists of a subset of the sinusoidal wrinkle modes at the first bifurcation, so the present study considers Field SC to be a meaningless field.

4.3. Cognate bifurcation modes obtained by superposition

The second bifurcation is multiple such as $k^{(2)}$=2 for Fields HA and SB, $k^{(2)}$=3 for Fields HB and HC, and $k^{(2)}$=4 for Field SA, because the obtained bifurcation modes (Figs. 8 and 9) consist of the sets of the identical bifurcation modes extended by the translational and/or rotational symmetries (Section 4.1). Thus, combination of the subsets of the identical bifurcation modes gives the variation of distinctive bifurcation modes. These modes are defined as the cognate modes with the basic mode. For simplicity, the present study considers the cognate modes obtained as below: the modes included in each subset have the same magnitude (i.e., $|r_i^{(2)}|=|r_j^{(2)}|$ in Eq. (6)) whereas the modes excluded from the subset have $r_m^{(2)}=0$. The cognate bifurcation modes obtained in the individual fields are shown in Figs. 12 and 13.

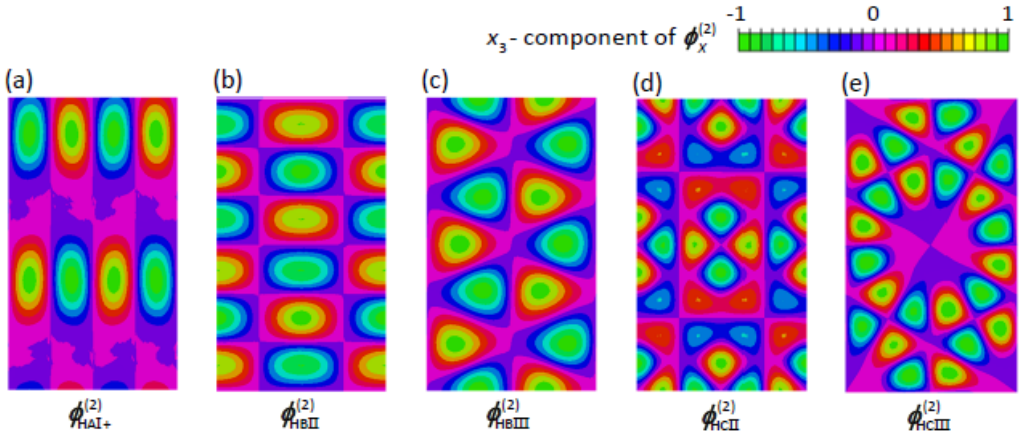

Fig. 12. Cognate bifurcation modes occurring in Fields HA, HB and HC. (a) Mode HAI+ (e.g., $\phi_{HAI+}^{(2)} = \phi_{HA0a}^{(2)} + \phi_{HA0b}^{(2)}$), (b) Mode HBII (e.g., $\phi_{HBII}^{(2)} = \phi_{HB60}^{(2)} + \phi_{HB60*}^{(2)}$), (c) Mode HBIII (e.g., $\phi_{HBIII}^{(2)} = \phi_{HB0}^{(2)} + \phi_{HB60}^{(2)} - \phi_{HB60*}^{(2)}$), (d) Mode HCII (e.g., $\phi_{HCII}^{(2)} = \phi_{HC60}^{(2)} - \phi_{HC60*}^{(2)}$), and (e) Mode HCIII (e.g., $\phi_{HCIII}^{(2)} = -\phi_{HC0}^{(2)} + \phi_{HC60}^{(2)} + \phi_{HC60*}^{(2)}$). Modes HAI, HBI and HCI are depicted as $\phi_{HAI}^{(2)} = \phi_{HA0a}^{(2)}$ (Fig. 8a), $\phi_{HBI}^{(2)} = \phi_{HB0}^{(2)}$ (Fig. 8c), and $\phi_{HCI}^{(2)} = \phi_{HC0}^{(2)}$ (Fig. 8f). Although the basic bifurcation modes are wavelike and occur in the symmetric directions (Fig. 8), superposition allows the cognate modes to become distinctive and diverse. Note that $\phi_{HAI+}^{(2)} = \phi_{HA0a}^{(2)} + \phi_{HA0b}^{(2)}$ is different from $\phi_{HAI}^{(2)}$. In addition, 4×4 unit cell analysis is needed to obtain $\phi_{HA60a,b,60*a,b}^{(2)}$, which are used to describe Modes HA(II, II+, III, III+,…) (Appendix B).

Fig. 12 shows the cognate bifurcation modes obtained for Fields H(A–C). First, when the combination of $c_1\phi_{HB0}^{(2)} + c_2\phi_{HB60}^{(2)} + c_3\phi_{HB60*}^{(2)}$ as c_i=(−1 or 0 or 1) is analyzed, Field HB is found to have the three symmetrically different modes, Modes HB(I, II, and III). This means that the cognate modes with $\phi_{HBI}^{(2)} = \phi_{HB0}^{(2)}$ (Mode HBI, Fig. 8c) are $\phi_{HBII}^{(2)} = \phi_{HB60}^{(2)} + \phi_{HB60*}^{(2)}$ (Mode HBII, Fig. 12b) and $\phi_{HBIII}^{(2)} = \phi_{HB0}^{(2)} + \phi_{HB60}^{(2)} - \phi_{HB60*}^{(2)}$ (Mode HBIII, Fig. 12c). Note that different signs of the coefficients do not generate different modes because the generated modes are periodically identical. The signs have been selected to make the cognate modes easier to recognize (Fig. 12). As a matter of course, Modes HB(I, II, and III) ($\phi_{HB(I,II,III)}^{(2)}$) are different so that evolution of different deformation patterns occurs on the different bifurcated paths regarded as the second bifurcated path. In the same way, Fig. 12d,e shows that Field HC has Modes HC(I, II, and III) so that $\phi_{HCII}^{(2)} = \phi_{HC60}^{(2)} - \phi_{HC60*}^{(2)}$ and $\phi_{HCIII}^{(2)} = -\phi_{HC0}^{(2)} + \phi_{HC60}^{(2)} + \phi_{HC60*}^{(2)}$ are cognate with $\phi_{HCI}^{(2)} = \phi_{HC0}^{(2)}$ (Fig. 8f). These cognate modes (Fig. 12b–e) appear because of the rotational symmetry of the hexagonal dimple pattern.

In contrast, Field HA has $k^{(2)}$=2 and two identical modes with a rectangular

checkerboard extended by the translational symmetry in the x_2 direction (Fig. 8a,b). Surprisingly, superposition of the two identical modes generates a different bifurcation mode ($\phi^{(2)}_{\mathrm{HA0a}}+\phi^{(2)}_{\mathrm{HA0b}}$, Fig. 12a) that is cognate with the individual modes ($\phi^{(2)}_{\mathrm{HA0a,b}}$, Fig. 8a,b). Thus, the cognate mode $\phi^{(2)}_{\mathrm{HA0a}}+\phi^{(2)}_{\mathrm{HA0b}}$ is categorized as Mode HAI+, which is different from $\phi^{(2)}_{\mathrm{HA0a,b}}$ as Mode HAI. In the case of Field HA, the 4×4 unit cell is needed to obtain the identical modes occurring in the symmetric directions because of the rotational symmetry (Appendix B). The combination of the obtained identical modes, $\phi^{(2)}_{\mathrm{HA60a,b,60*a,b}}$, generates the cognate modes as Modes HA(II, II+, III, and III+). Although other combinations, except for Modes HA(I, I+, II, II+, III, and III+), are also obtainable (Appendix B), the present study mainly focuses on analyzing pattern evolution from Modes HA(I and I+) because the 4×4 unit cell requires tremendous computational cost to consider many cognate modes. Comparison of Figs. 8 and 12 shows that superposition allows the cognate modes to become diverse and distinctive. The second bifurcation is found to promise evolution from the hexagonal dimple pattern to a variation of the deformation patterns caused by Modes HA(I and I+,…), HB(I, II, and III) and HC(I, II, and III) (Section 5).

Fig. 13 shows the cognate bifurcation modes obtained by considering Fields SA and SB. When the cognate modes in Field SA ($k^{(2)}$=4) are also systematically considered by investigating the combination of $c_1\phi^{(2)}_{\mathrm{SA0a}}+c_2\phi^{(2)}_{\mathrm{SA0b}}+c_3\phi^{(2)}_{\mathrm{SA90a}}+c_4\phi^{(2)}_{\mathrm{SA90b}}$ as c_i=(−1 or 0 or 1), Modes SA(I, I+, II, II+, III, and IV) (Fig. 13a–e) are recognized as the different modes in Field SA (i.e., six different modes). Modes SA(I, I+, II, II+, III, and IV) are obtained, for instance, by $\phi^{(2)}_{\mathrm{SAI}}=\phi^{(2)}_{\mathrm{SA0a}}$ (Fig. 9a), $\phi^{(2)}_{\mathrm{SAI+}}=\phi^{(2)}_{\mathrm{SA0a}}+\phi^{(2)}_{\mathrm{SA0b}}$ (Fig. 13a), $\phi^{(2)}_{\mathrm{SAII}}=\phi^{(2)}_{\mathrm{SA0b}}-\phi^{(2)}_{\mathrm{SA90b}}$ (Fig. 13b), $\phi^{(2)}_{\mathrm{SAII+}}=\phi^{(2)}_{\mathrm{SA0a}}+\phi^{(2)}_{\mathrm{SA90b}}$ (Fig. 13c), $\phi^{(2)}_{\mathrm{SAIII}}=\phi^{(2)}_{\mathrm{SA0a}}+\phi^{(2)}_{\mathrm{SA0b}}+\phi^{(2)}_{\mathrm{SA90a}}$ (Fig. 13d), and $\phi^{(2)}_{\mathrm{SAIV}}=\phi^{(2)}_{\mathrm{SA0a}}+\phi^{(2)}_{\mathrm{SA0b}}+\phi^{(2)}_{\mathrm{SA90a}}+\phi^{(2)}_{\mathrm{SA90b}}$ (Fig. 13e). In contrast, Field SB simply produces the cognate bifurcation mode as $\phi^{(2)}_{\mathrm{SB45}}+\phi^{(2)}_{\mathrm{SB45*}}$ because $k^{(2)}$=2. Modes SB(I and II) are expressed as $\phi^{(2)}_{\mathrm{SBI}}=\phi^{(2)}_{\mathrm{SB45}}$ (Fig. 9e) and $\phi^{(2)}_{\mathrm{SBII}}=\phi^{(2)}_{\mathrm{SB45}}+\phi^{(2)}_{\mathrm{SB45*}}$ (Fig. 13f). Evolution from the square dimple pattern is also expected to generate the complex and diverse deformation patterns caused by Modes SA(I, I+, II, II+, III, and IV) and SB(I and II) (Section 5).

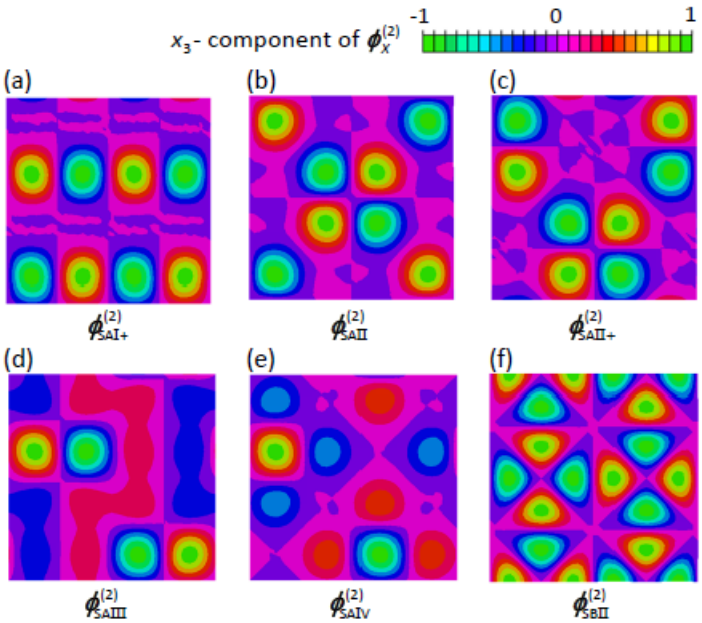

Fig. 13. Cognate bifurcation modes occurring in Fields SA and SB. (a) Mode SAI+ (e.g., $\phi_{SAI+}^{(2)} = \phi_{SA0a}^{(2)} + \phi_{SA0b}^{(2)}$), (b) Mode SAII (e.g., $\phi_{SAII}^{(2)} = \phi_{SA0b}^{(2)} - \phi_{SA90b}^{(2)}$), (c) Mode SAII+ (e.g., $\phi_{SAII+}^{(2)} = \phi_{SA0a}^{(2)} + \phi_{SA90b}^{(2)}$), (d) Mode SAIII (e.g., $\phi_{SAIII}^{(2)} = \phi_{SA0a}^{(2)} + \phi_{SA0b}^{(2)} + \phi_{SA90a}^{(2)}$), (e) Mode SAIV (e.g., $\phi_{SAIV}^{(2)} = \phi_{SA0a}^{(2)} + \phi_{SA0b}^{(2)} + \phi_{SA90a}^{(2)} + \phi_{SA90b}^{(2)}$), and (f) Mode SBII (e.g., $\phi_{SBII}^{(2)} = \phi_{SB45}^{(2)} + \phi_{SB45*}^{(2)}$). Modes SAI and SBI are depicted as $\phi_{SAI}^{(2)} = \phi_{SA0a}^{(2)}$ (Fig. 9a) and $\phi_{SBI}^{(2)} = \phi_{SB45}^{(2)}$ (Fig. 9e). Note that $\phi_{SAII}^{(2)}$ and $\phi_{SAII+}^{(2)}$ are periodically identical but recognized as different modes because different imperfections are generated by superposition of the modes at the first and second bifurcations (Fig. 17).

5. Evolution of deformation patterns on the second bifurcated path

Figs. 14–18 show pattern evolution on the second bifurcated path for Fields HA, HB, HC, SA and SB, respectively. The individual figures compare the imperfection consisting of the first and second bifurcation modes, such as $\phi_{HEX}^{(1)} + \phi_{HAI}^{(2)}$ (Eq. (6)), with deformation pattern evolution as a function of σ_0 / σ_0^c. Although the basic modes at the second bifurcations are basically wavelike, such as the stripe and rectangular checkerboard modes (Section 4.1), when the cognate modes (Section 4.3) interact with the first bifurcation (i.e., with the hexagonal and square dimples, Section 3.4), the deformation patterns successfully reproduce herringbone patterns as well as diverse and distinctive patterns, including the experimentally observed patterns (Breid and Crosby, 2011; Guvendiren et al., 2009). In addition, each bifurcation mode obtained at the second bifurcation point (Figs. 8, 9, 12 and 13) does not seem to be responsible to

pattern evolution on the second bifurcated path (Healey, 1989), the imperfection obtained from superposition of the dominant modes at the first and second bifurcation points (Eq. (6)) successfully explains pattern evolution on the second bifurcated path (Miyoshi et al., 2021), i.e., accidental path switching does not occur in these case.

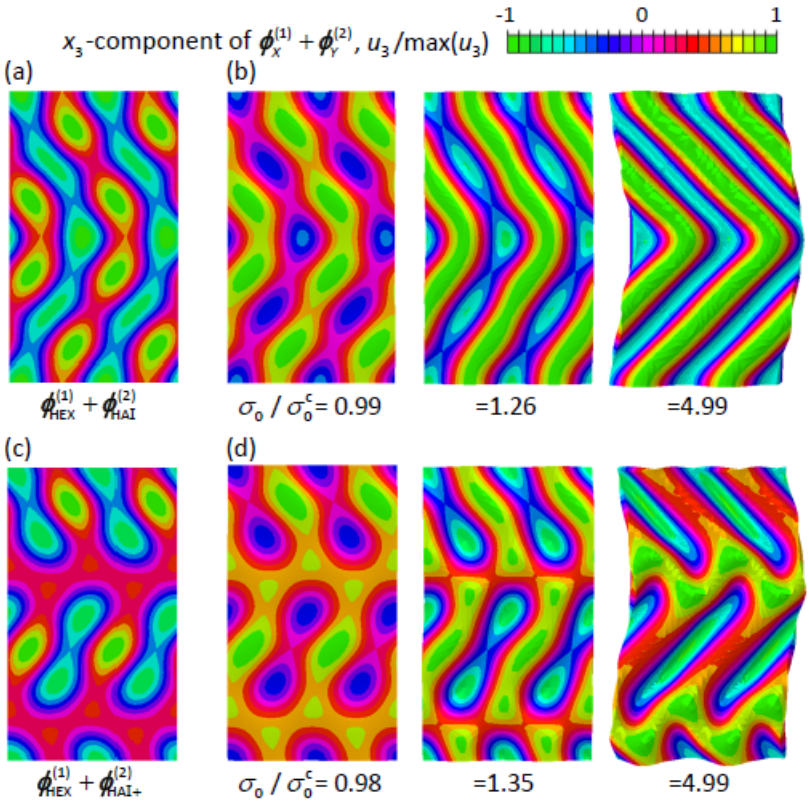

Fig. 14. Initial imperfection and evolution of the deformation pattern from Modes HA(I and I+). (a) Initial imperfection ($\phi_{HEX}^{(1)}+\phi_{HAI}^{(2)}$) and (b) the corresponding deformation pattern. (c) Initial imperfection ($\phi_{HEX}^{(1)}+\phi_{HAI+}^{(2)}$) and (d) the corresponding deformation pattern. The parameter set of $\{L_2/L_1,\ E_f/E_s,\ d^{(1)}/h\}=\{\sqrt{3},\ 20,\ 0.01(=d^{(2)}/h)\}$ is used as the representative in Field HA. Modes HA(I and I+) cause coalescence of dimples, evolving from the hexagonal dimples to herringbone and peanut patterns on the second bifurcated path. These patterns are the cognate patterns caused by the second bifurcation in Field HA.

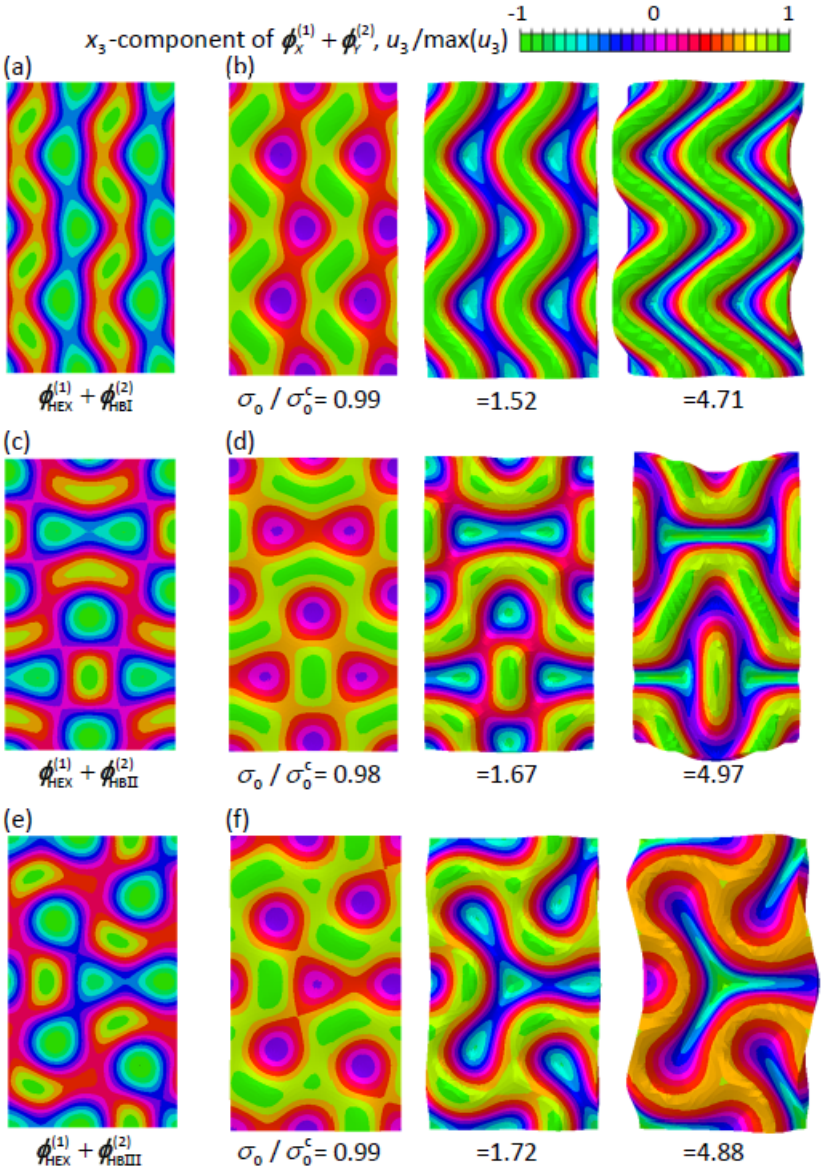

Fig. 15. Initial imperfection and evolution of the deformation pattern from Modes HB(I, II, and III). (a) Initial imperfection ($\phi_{HEX}^{(1)} + \phi_{HBI}^{(2)}$) and (b) the corresponding deformation pattern. (c) Initial imperfection ($\phi_{HEX}^{(1)} + \phi_{HBII}^{(2)}$) and (d) the corresponding deformation pattern. (e) Initial imperfection ($\phi_{HEX}^{(1)} + \phi_{HBIII}^{(2)}$) and (f) the corresponding deformation pattern. The parameter set of $\{L_2/L_1, E_f/E_s, d^{(1)}/h\}=\{\sqrt{3}, 9, 0.01(=d^{(2)}/h)\}$ is used as the representative in Field HB. Modes HB(I, II, and III) cause coalescence of dimples, evolving from the hexagonal dimples to herringbone, zipper and triple-junction patterns on the second bifurcated path (Breid and Crosby, 2011; Tallinen and Biggins, 2015). Remarkably, these patterns are the cognate patterns caused by the second bifurcation in Field HB.

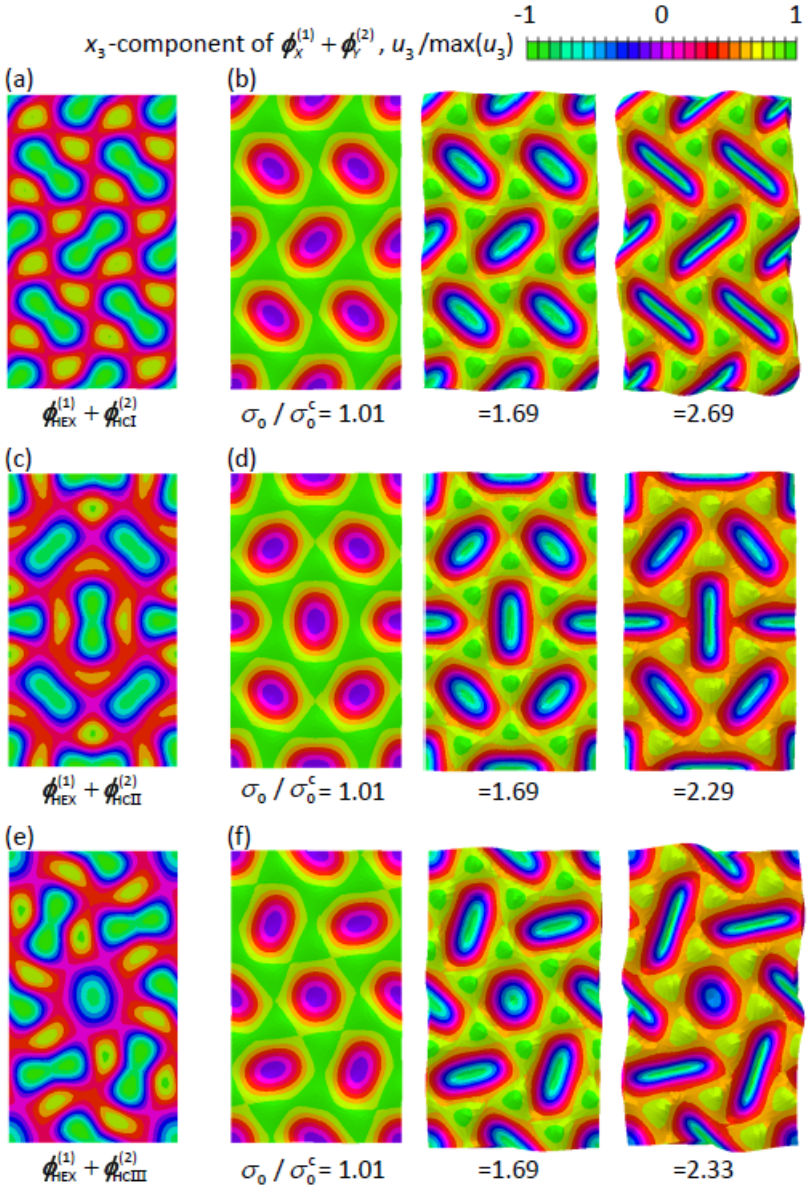

Fig. 16. Initial imperfection and evolution of the deformation pattern from Modes HC(I, II, and III). (a) Initial imperfection ($\phi_{HEX}^{(1)} + \phi_{HCI}^{(2)}$) and (b) the corresponding deformation pattern. (c) Initial imperfection ($\phi_{HEX}^{(1)} + \phi_{HCII}^{(2)}$) and (d) the corresponding deformation pattern. (e) Initial imperfection ($\phi_{HEX}^{(1)} + \phi_{HCIII}^{(2)}$) and (f) the corresponding deformation pattern. The parameter set of $\{L_2/L_1,\ E_f/E_s,\ d^{(1)}/h\} = \{\sqrt{3},\ 6,\ 0.01(=d^{(2)}/h)\}$ is used as the representative in Field HC. As elucidated by Miyoshi et al. (2021), Modes HC(I, II, and III) give distorted dimples (not coalescence), evolving from the hexagonal dimples to brick- and cage- like patterns on the second bifurcated path. Further, when focusing on the periodic arrangement of the distorted dimples, the periodic arrangement has an analogy with the in-plane buckling behavior of hexagonal honeycombs (Ohno et al., 2002; Okumura et al., 2002). Note that further bifurcations are needed for occurrence of herringbone and labyrinth patterns (Miyoshi et al., 2021).

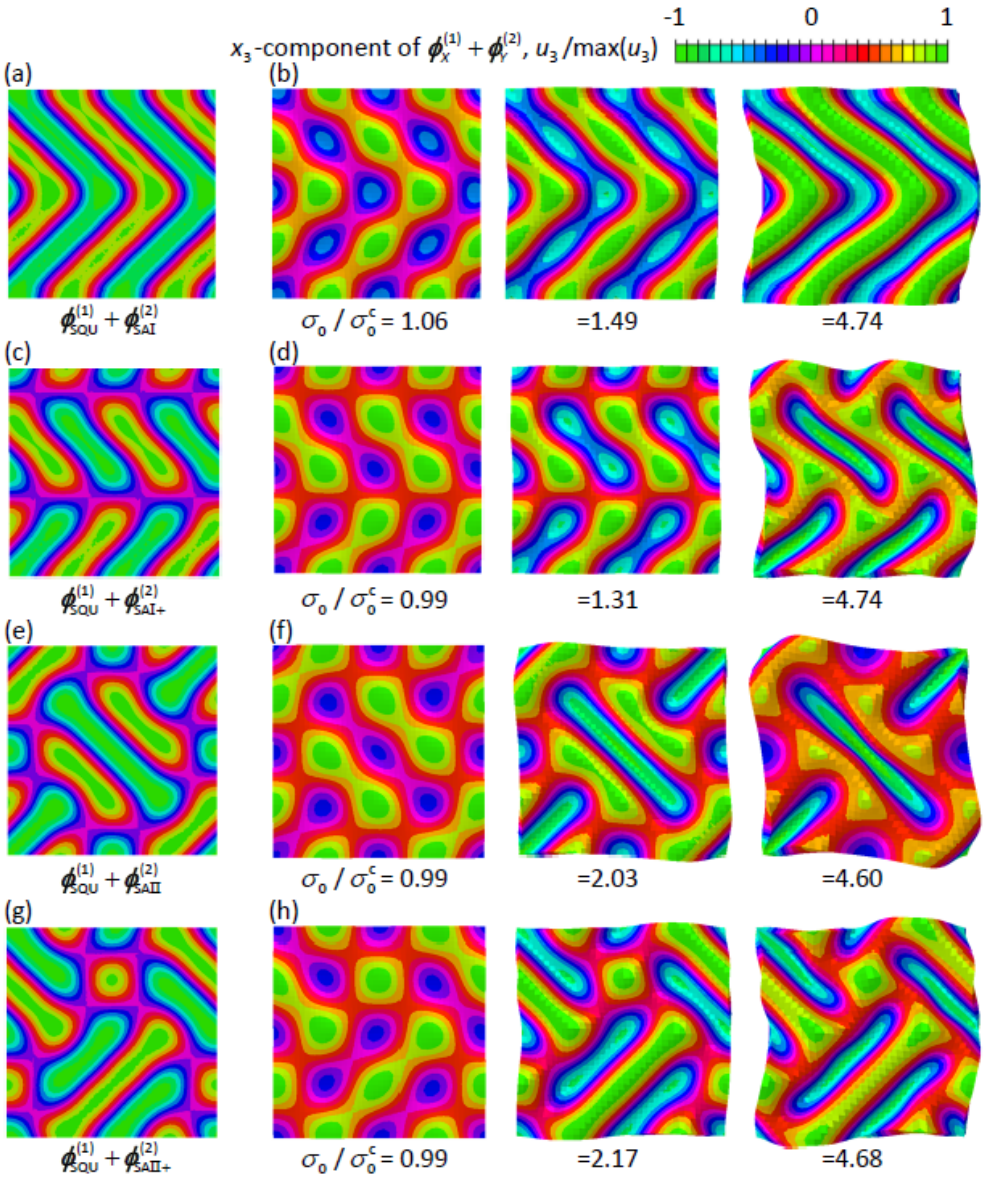

Fig. 17. Initial imperfection and evolution of the deformation pattern from Modes SA(I, I+, II, and II+). (a) Initial imperfection ($\phi_{SQU}^{(1)} + \phi_{SAI}^{(2)}$) and (b) the corresponding deformation pattern. (c) Initial imperfection ($\phi_{SQU}^{(1)} + \phi_{SAI+}^{(2)}$) and (d) the corresponding deformation pattern. (e) Initial imperfection ($\phi_{SQU}^{(1)} + \phi_{SAII}^{(2)}$) and (f) the corresponding deformation pattern. (g) Initial imperfection ($\phi_{SQU}^{(1)} + \phi_{SAII+}^{(2)}$) and (h) the corresponding deformation pattern. The parameter set of $\{L_2/L_1, E_f/E_s, d^{(1)}/h\}=\{1, 15, 0.01(=d^{(2)}/h)\}$ is used as the representative in Field SA. Modes SA(I, I+, II, and II+) cause coalescence of dimples depending on the individual modes. Modes SA(I and I+) result in herringbone and peanut patterns, which are similar to the response of Modes HA(I and I+), whereas Modes SA(II and II+) result in two types of weave patterns (i.e., plane and basket weave patterns, Fig. 2e,f), which can also be viewed as diamond plate patterns (Okumura et al., 2015). The plane weave pattern caused by Mode SAII corresponds to the pattern observed in the experiments of Breid and Crosby (2011). The diversity of the obtained patterns is understood as a result of the cognate patterns caused by the second bifurcation in Field SA.

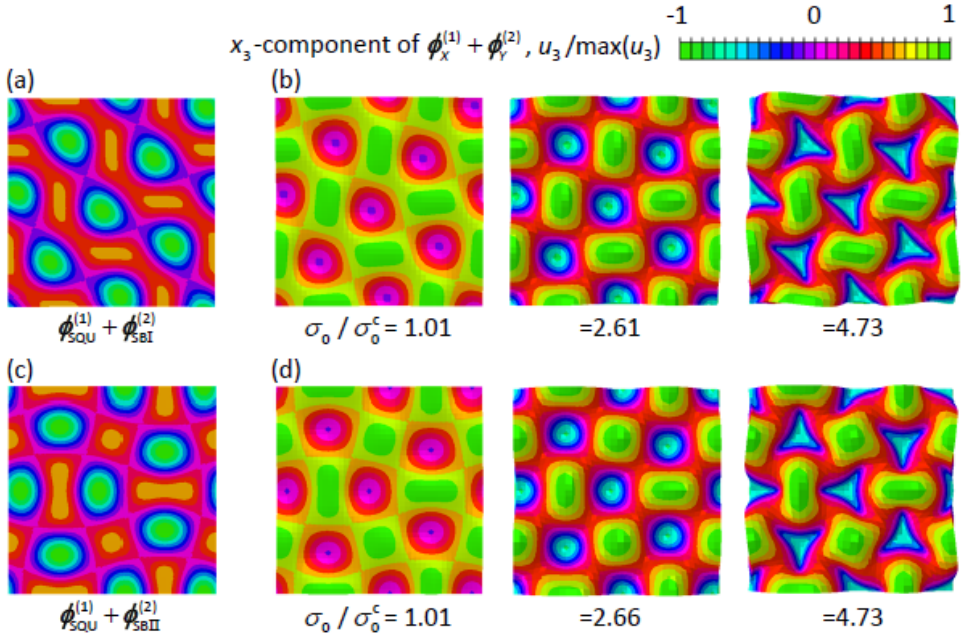

Fig. 18. Initial imperfection and evolution of deformation pattern from Modes SB(I and II). (a) Initial imperfection ($\phi_{SQU}^{(1)} + \phi_{SBI}^{(2)}$) and (b) the corresponding deformation pattern. (c) Initial imperfection ($\phi_{SQU}^{(1)} + \phi_{SBII}^{(2)}$) and (d) the corresponding deformation pattern. The parameter set of $\{L_2/L_1, E_f/E_s, d^{(1)}/h\}=\{1, 5, 0.01(=d^{(2)}/h)\}$ is used as the representative in Field SB. Modes SB(I and II) distort the circular dimples to triangular dimples. When focusing on the shape and periodic arrangement of the bumps instead of the dimples, the morphology has an analogy with the in-plane buckling behavior of square honeycombs (Ohno et al., 2004).

A variety of herringbone patterns with different dimensions appear on the second bifurcated paths induced by Modes HAI (Fig. 14a,b), HBI(Fig. 15a,b), and SAI (Fig. 17a,b). The second bifurcations play a role in causing coalescence of the selected combination of dimples. Sequential combination of the first and second bifurcations evolves from the dimple patterns to the herringbone patterns with different dimensions (cf. Chen and Hutchinson, 2004; Miyoshi et al., 2021). Occurrence and evolution of the herringbone patterns occur in the broad range of Fields HA, HB, and SA. Fields HC and SB also give a herringbone pattern on the third bifurcated path (not on the second bifurcated path) (see Section 6). Further, surprisingly, the experimentally and numerically observed distinctive patterns appear from Modes HAI+, HB(II and III), and SA(I+, II, and II+), which are generated as the cognate modes of Modes HAI, HBI, and SAI (these modes lead to the herringbone patterns), respectively. The peanut patterns (Breid and Crosby, 2011; Guvendiren et al., 2009) occur from Modes HAI+ and SAI+ (Figs. 14c,d and 17c,d). The triple-junction pattern (Tallinen and Biggins, 2015) appears

from Mode HBIII (Fig. 15e,f), whereas the zipper pattern (Breid and Crosby, 2011) appears from Mode HBII (Fig. 15c,d). Further, the plane and basket weave patterns (Breid and Crosby, 2011) occur from Modes SA(II and II+) (Fig. 17e–h). Because the cognate bifurcation modes (Figs. 12 and 13) are generated by superposition of the basic bifurcation modes in the symmetric directions (Figs. 8 and 9), these diverse and distinctive patterns are understood as cognate patterns with the herringbone pattern. This unbelievable but reasonable interpretation is one of the key findings of the present study.

Although Fields HA, HB, and SA give the herringbone pattern and its cognate patterns, such as the peanut, triple-junction, weave and zipper patterns, on the second bifurcated path, Fields HC and SB show different responses (Figs. 16 and 18). As reported by Miyoshi et al. (2021), Modes HC(I, II, and III) have an analogy with the in-plane buckling behavior of hexagonal honeycombs, i.e., the first bifurcation yields a hexagonal dimple structure, whereas the second bifurcation produces the periodic arrangement of the distorted dimples (not coalescence of dimples), which have an analogy with the uniaxial, biaxial, and equibiaxial (flower-like) patterns (Gibson and Ashby, 1997; Papka and Kyriakides, 1999; Ohno et al., 2002; Combescure et al., 2020). The resulting deformation patterns are recognized as the brick- and cage-like patterns experimentally reported by Breid and Crosby (2011). The third and/or fourth bifurcations need to evolve from these intermediate patterns (Fig. 16) to the herringbone and labyrinth patterns (Miyoshi et al., 2021, Section 6). In the same way, the deformation patterns caused by Modes SB(I and II) (Fig. 18) do not include the herringbone pattern, and they are also understood to be intermediate patterns, which affect evolution of the deformation patterns on the third bifurcated path (Section 6). In addition, Modes SB(I and II) distort the circular dimples to triangular dimples. When focusing on the shape and periodic arrangement of the bumps instead of the triangular dimples, the morphology has an analogy with the in-plane buckling behavior of square honeycombs (Ohno et al., 2004). Pattern evolution from the intermediate patterns of Modes HC(I, II, and III) and SB(I and II) will be discussed in Section 6.

It is additionally noted that analysis of pattern evolution from Modes SA(III and IV)

caused accidental path switching (Healey, 1989), leading to the herringbone and plane weave patterns obtained by Modes SA(I and II), respectively (Fig. 17b,f). Although the imperfections generated from Modes SA(III and IV) are not shown here to avoid redundancy, the imperfection from Mode SAIII seems to evolve to an extended herringbone pattern whereas the imperfection from Mode SAIV seems to evolve to a mixed pattern of the plane and basket weave patterns. This implies that the bifurcated paths from Modes SA(III and IV) are similar to those from Modes SA(I and II), respectively, as well as that Modes SA(III and IV) are energetically inferior to Modes SA(I and II), respectively. The postbuckling analysis using Modes SA(III and IV) may be achieved by introducing additional constraints (Okumura et al., 2002). In addition, as demonstrated by Pandurangi et al. (2020), all the bifurcated paths regardless of the lowest and higher-order bifurcation points can be traced by analysis of the perfect system using group-theoretic methods (Sattinger, 1979; Golubitsky et al., 1988; Healey, 1988). However, we consider such analysis to be out of the scope in the present study.

6. Discussion

6.1. Decrease of the elastic energy from on the first bifurcated path

Fig. 19 shows the decrease of U/U_0 from on the first bifurcated path when Modes HA(I and I+), HB(I, II, and III), HC(I, II, and III), SA(I, I+, II, and II+), and SB(I and II) are used to obtain the corresponding second bifurcated paths. A clear decrease of U/U_0 occurs for Modes HA(I and I+), HB(I, II, and III) and SA(I, I+, II, and II+) (Fig. 19a,b,d), while a slight decrease is caused by Modes HC(I, II, and III) and SB(I and II) (Fig. 19c,e). The former group includes the herringbone and cognate patterns, which play a considerable role in releasing the elastic energy stored on the first bifurcated path. In addition, the energy decreases of the herringbone and cognate patterns are almost the same (although the herringbone patterns are slightly superior to the cognate patterns), i.e., the cognate patterns are also dominant on the second bifurcated path. This result gives a reasonable explanation for the analysis of the triple-junction pattern by Tallinen and Biggins (2015) and the experimental observation by Breid and Crosby (2009, 2011). In contrast, the latter group (Modes HC(I, II, and III) and SB(I and II)) is considered as intermediate patterns that do not include the herringbone pattern (Figs. 16 and 18), i.e., further bifurcations can cause a further decrease of the elastic energy with pattern

evolution. These possibilities will be shown in Section 6.2.

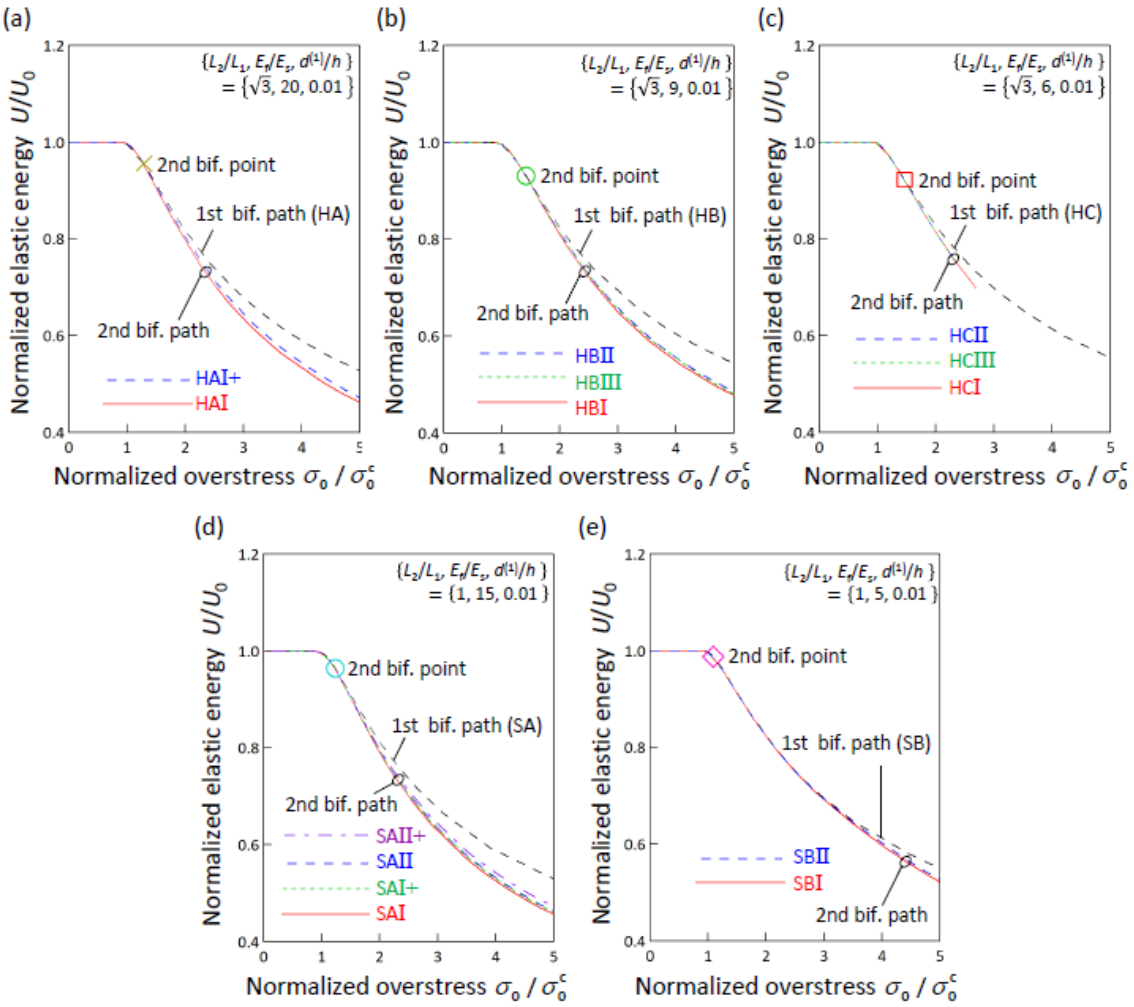

Fig. 19. Decrease of U/U_0 as a function of σ_0 / σ_0^c from on the first bifurcated path for (a) Modes HA(I and I+), (b) Modes HB(I, II, and III), (c) Modes HC(I, II, and III), (d) Modes SA(I, I+, II, and II+), and (e) Modes SB(I and II). Modes HAI, HB(I, II, and III), and Modes SA(I, I+, II, and II+) include the herringbone pattern and its cognate patterns (Figs. 14, 15 and 17). The energy decreases of the herringbone and cognate patterns are almost the same, i.e., the cognate patterns are also dominant compared with the herringbone pattern. There is a clear energy decrease in these cases. In contrast, Modes HC(I, II, and III) and SB(I and II) do not include the herringbone pattern and give intermediate patterns (Figs. 16 and 18), leading to a slight decrease of the elastic energy. Further bifurcations may cause a further decrease of the elastic energy with pattern evolution.

6.2. Third bifurcation analysis from Modes HC(I, II, and III) and SB(I and II)

The bifurcation mode, the imperfection, and the deformation pattern obtained by analysis of the third bifurcation on the second bifurcated paths obtained by Modes HC(I,

II, and III) are shown in Fig. 20. The multiplicity of the bifurcations is $k^{(3)}$=1 for the three cases. The bifurcation modes ($\boldsymbol{\phi}^{(3)}_{\mathrm{HCI}}$, $\boldsymbol{\phi}^{(3)}_{\mathrm{HCII}}$, and $\boldsymbol{\phi}^{(3)}_{\mathrm{HCIII}}$, Fig. 20a,d,g) can be understood as Modes HB(I, II, and III) (Figs. 8c and 12b,c) being distorted by the deformation pattern of Modes HC(I, II, and III), respectively. Fig. 20 indicates that evolution of the intermediate patterns by Modes HC(I and III) does not prevent occurrence of the herringbone and triple-junction patterns, but Mode HCII loses the chance of occurrence of the zipper pattern (cf. Fig. 15). Especially, Fig. 20i is viewed as the asymmetric triple-junction pattern reported by Tallinen and Biggins (2015). These responses support the robustness of the herringbone pattern and the diversity of the cognate patterns. According to Miyoshi et al. (2021), the occurrence of the fourth bifurcation allows the cognate patterns (Fig. 20f,i) to become the periodical labyrinth pattern.

The responses of the third bifurcation from Modes SB(I and II) are shown in Fig. 21. Both cases have $k^{(3)}$=2 with $\boldsymbol{\phi}^{(3)}_{\mathrm{SBIa}}$ and $\boldsymbol{\phi}^{(3)}_{\mathrm{SBIb}}$ (Fig. 21a,b) for Mode SBI and $\boldsymbol{\phi}^{(3)}_{\mathrm{SBII0a}}$ and $\boldsymbol{\phi}^{(3)}_{\mathrm{SBII90b}}$ (Fig. 21h,i) for Mode SBII. Thus, the cognate modes are expressed as $\boldsymbol{\phi}^{(3)}_{\mathrm{SBIa}}+\boldsymbol{\phi}^{(3)}_{\mathrm{SBIb}}$ (Fig. 21e) and $\boldsymbol{\phi}^{(3)}_{\mathrm{SBII0a}}+\boldsymbol{\phi}^{(3)}_{\mathrm{SBII90b}}$ (Fig. 21l), respectively. When these modes are compared with Modes SA(I, I+, II, II+, III, and IV) (Figs. 9a–d and 13a–e), the third bifurcation modes are found to be subsets of Modes SA(I, I+, II, II+, III, and IV), although the obtained modes are slightly distorted by evolution of the deformation patterns caused by Modes SB(I and II). This is the reason why $k^{(2)}$=4 for Field SA reduces to $k^{(3)}$=2 at the third bifurcation from Modes SB(I and II). The third bifurcation from Mode SBI results in evolution of a plane weave pattern (Fig. 21c,d, see Fig. 2e), which is caused by $\boldsymbol{\phi}^{(3)}_{\mathrm{SBIa}}$ or $\boldsymbol{\phi}^{(3)}_{\mathrm{SBIb}}$ (cf. Mode SAII for Field SA), whereas the cognate pattern caused by $\boldsymbol{\phi}^{(3)}_{\mathrm{SBIa}}+\boldsymbol{\phi}^{(3)}_{\mathrm{SBIb}}$ (cf. Mode SAIV for Field SA) is a mixed (i.e., plane and basket) weave pattern (Fig. 21f,g). Further, the third bifurcation from Mode SBII leads to evolution of the herringbone pattern (Fig. 21j,k) caused by $\boldsymbol{\phi}^{(3)}_{\mathrm{SBII0a}}$ or $\boldsymbol{\phi}^{(3)}_{\mathrm{SBII90b}}$, because these modes correspond to Mode SAI for Field SA, whereas $\boldsymbol{\phi}^{(3)}_{\mathrm{SBII0a}}+\boldsymbol{\phi}^{(3)}_{\mathrm{SBII90b}}$ (Mode SAII+ for Field SA) causes evolution of a basket weave pattern (Fig. 21m,n, see Fig. 2f). Field SB also has a herringbone pattern (Fig. 21k), as well as three types of distorted weave patterns (Fig. 21d,g,n).

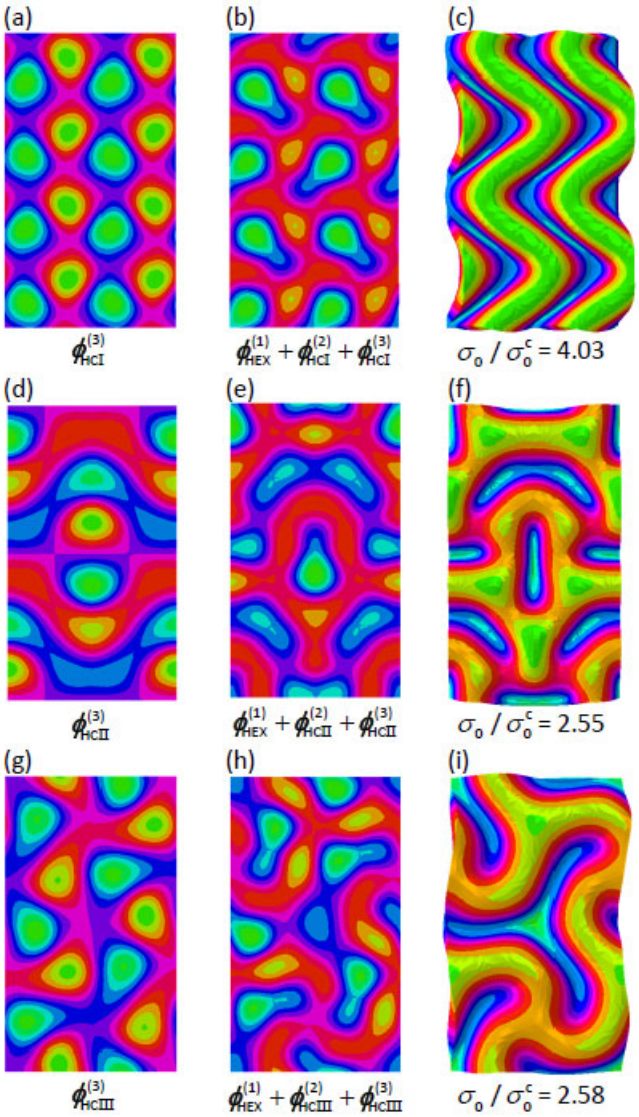

Fig. 20. Responses of the third bifurcation analyzed on the second bifurcated paths obtained by Modes HC(I, II, and III). (a) $\phi_{\mathrm{HCI}}^{(3)}$, (b) $\phi_{\mathrm{HEX}}^{(1)}+\phi_{\mathrm{HCI}}^{(2)}+\phi_{\mathrm{HCI}}^{(3)}$, and (c) the corresponding deformation pattern. (d) $\phi_{\mathrm{HCII}}^{(3)}$, (e) $\phi_{\mathrm{HEX}}^{(1)}+\phi_{\mathrm{HCII}}^{(2)}+\phi_{\mathrm{HCII}}^{(3)}$, and (f) the corresponding deformation pattern. (g) $\phi_{\mathrm{HCIII}}^{(3)}$, (h) $\phi_{\mathrm{HEX}}^{(1)}+\phi_{\mathrm{HCIII}}^{(2)}+\phi_{\mathrm{HCIII}}^{(3)}$, and (i) the corresponding deformation pattern. The parameter set of $\{L_2/L_1,\ E_\mathrm{f}/E_\mathrm{s},\ d^{(1)}/h\}=\{\sqrt{3},\ 6,\ 0.01(=d^{(2)}/h=d^{(3)}/h)\}$ is used. The individual modes ($k^{(3)}=1$) correspond to Modes HB(I, II, and III), but they are distorted by the deformation patterns on the second bifurcated path induced by Modes HC(I, II, and III). Pattern evolution by Modes HC(I and III) does not prevent occurrence of the herringbone and triple-junction patterns, but Mode HCII loses the chance of occurrence of the zipper pattern. This supports the robustness of the herringbone pattern and the diversity of the cognate patterns.

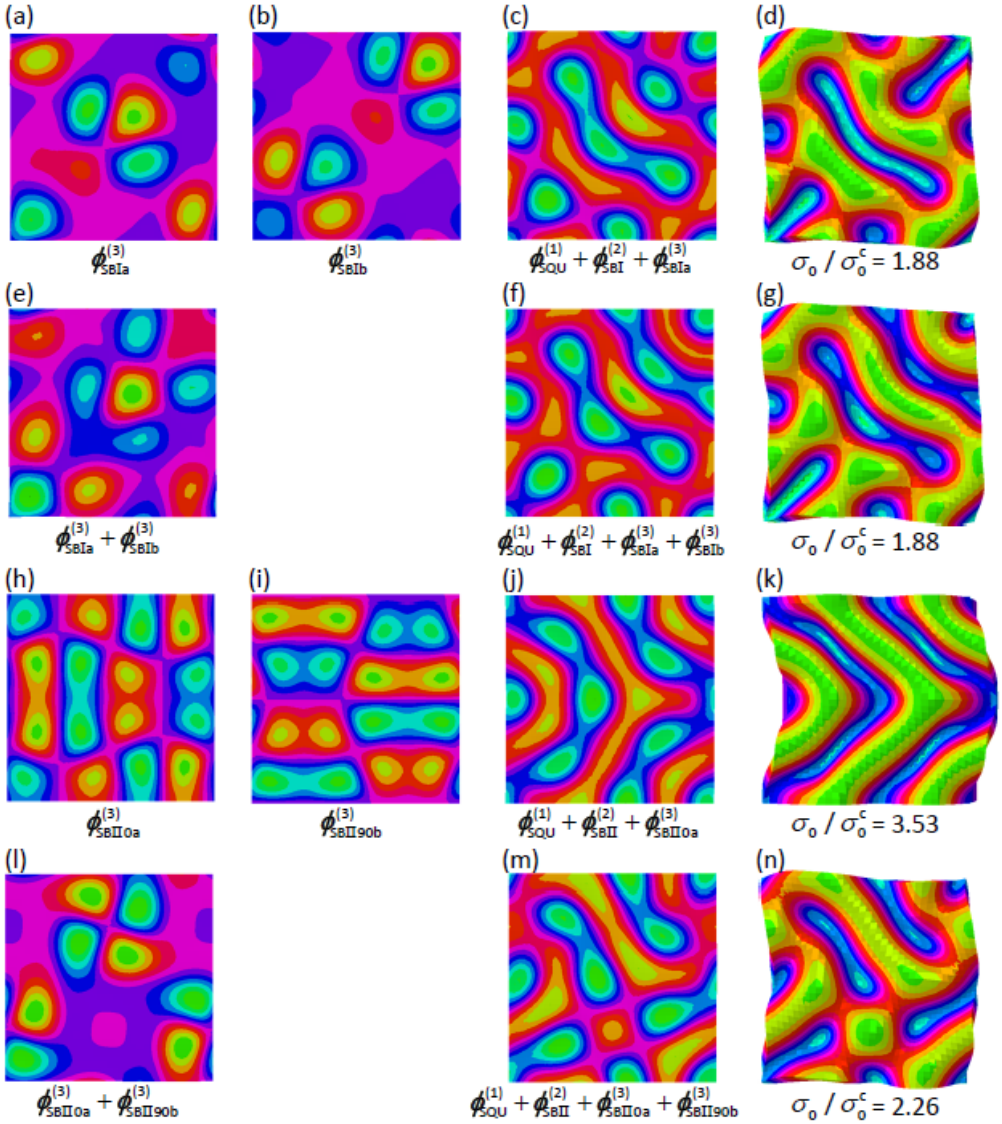

Fig. 21. Responses of the third bifurcation analyzed on the second bifurcated paths obtained by Modes SB(I and II). (a) $\phi^{(3)}_{SBIa}$, (b) $\phi^{(3)}_{SBIb}$, (c) $\phi^{(1)}_{SQU}+\phi^{(2)}_{SBI}+\phi^{(3)}_{SBIa}$, and (d) the corresponding deformation pattern. (e) $\phi^{(3)}_{SBIa}+\phi^{(3)}_{SBIb}$, (f) $\phi^{(1)}_{SQU}+\phi^{(2)}_{SBI}+\phi^{(3)}_{SBIa}+\phi^{(3)}_{SBIb}$, and (g) the corresponding deformation pattern. (h) $\phi^{(3)}_{SBII0a}$, (i) $\phi^{(3)}_{SBII90b}$, (j) $\phi^{(1)}_{SQU}+\phi^{(2)}_{SBII}+\phi^{(3)}_{SBII0a}$, and (k) the corresponding deformation pattern. (l) $\phi^{(3)}_{SBII0a}+\phi^{(3)}_{SBII90b}$, (m) $\phi^{(1)}_{SQU}+\phi^{(2)}_{SBII}+\phi^{(3)}_{SBII0a}+\phi^{(3)}_{SBII90b}$, and (n) the corresponding deformation pattern. The parameter set of $\{L_2/L_1,\ E_f/E_s,\ d^{(1)}/h\}=\{1,\ 5,\ 0.05(=d^{(2)}/h=d^{(3)}/h)\}$ is used. The bifurcation modes ($\phi^{(3)}_{SBIa}$, $\phi^{(3)}_{SBIa}+\phi^{(3)}_{SBIb}$, $\phi^{(3)}_{SBII0a}$, and $\phi^{(3)}_{SBII0a}+\phi^{(3)}_{SBII90b}$) are slightly distorted modes of Modes SA(II, IV, I, and II+), evolving to distorted weave and herringbone patterns. In field SB, the herringbone pattern can also appear and the plane, basket, and mixed weave patterns appear as the cognate patterns.

It is finally noted that clear energy differences between the herringbone and cognate patterns are not recognized for all cases. This could be because the present study considers the film and substrate to be incompressible with a relatively small Young's

modulus ratio in the range 2–20. As pointed out by Chen and Hutchinson (2004) and Cai et al. (2011), a very large Young's modulus ratio (approximately 1000–3000) gives a considerable difference in the energy decrease between the herringbone and other wavelike patterns. In contrast, as pointed out by Breid and Crosby (2011), Tallinen and Biggins (2015), and Campos et al. (2021), a small Young's modulus ratio (including that used in the present study) gives a variety of coexistence patterns because the energy differences are almost negligible and comparable. The present study elucidates that the herringbone patterns have the potential to occur in all of Fields HA, HB, HC, SA, and SB, and the triple-junction, weave, peanut, and zipper patterns also appear as cognate patterns with the herringbone pattern. Note that the analyzed weave patterns can be divided into the plane weave pattern (from Mode SAII, Figs. 2e, 17f, and 21d), the basket weave pattern (from Mode SAII+, Figs. 2f, 17h, and 21n), and the mixed weave pattern (from Mode SAIV, Fig. 21g). The plane weave pattern perfectly corresponds to the pattern observed by Breid and Crosby (2011).

7. Conclusions

We have investigated the diversity of the bifurcations and deformations during evolution of periodic patterns on compressed films bonded to compliant substrates. Step-by-step eigenvalue buckling analysis was performed to detect the dominant bifurcation points on the bifurcated paths whereas postbuckling analysis was performed using the imperfection prescribed by the set of dominant bifurcation modes. The second bifurcation was investigated as a function of the Young's modulus ratio, as well as the imperfection magnitude, elucidating the robustness of the herringbone pattern and the diversity of the distinctive patterns cognate with the herringbone pattern. The new findings are described below.

When the Young's modulus ratio was considered in the range 2–20, the second bifurcation was divided into Fields H(A–D) and S(A–C) for the hexagonal and square dimple patterns, respectively. To visualize the fields, the bifurcation mode diagrams were shown as a function of the Young's modulus ratio, as well as the imperfection magnitude (Figs. 10 and 11). The imperfection magnitude should be parameterized when imperfection methods are used to analyze the second and sequent bifurcations.

Fields HD and SC were regarded as the meaningless fields caused by the multiplicity of bifurcations at the first bifurcation point. The basic bifurcation modes were the rectangular checkerboard modes for Fields H(A and C) and S(A and B) and the stripe modes for Field HB (Figs. 8 and 9). The different basic modes in the individual fields gave a family of herringbone deformation patterns with different dimensions. The multiplicity of bifurcations was explained by the translational and rotational symmetries because of the hexagonal and square dimples patterns. Superposition of the identical modes in symmetric directions (i.e., the cognate modes, Figs. 12 and 13) demonstrated the existence of the distinctive patterns cognate with the herringbone patterns, i.e., the triple-junction, peanut, zipper and weave patterns were cognate with the herringbone pattern (Figs. 14–18, 20, and 21). The energy differences between the herringbone and cognate patterns were almost negligible and comparable (Fig. 19), so coexistence of diverse and distinctive patterns occurs. These impactful and sophisticated findings provide a deep understanding of the robustness of the herringbone patterns and the diversity of the distinctive patterns cognate with the herringbone patterns.

Note that the present study used the same imperfection magnitude of $d^{(1)}/h=d^{(2)}/h=d^{(3)}/h$ to analyze the second and third bifurcated paths (see Sections 5 and 6), i.e., the first bifurcated paths were investigated using the variables of $d^{(1)}/h$ as an additional parameter. If the values of $d^{(2)}/h$ and $d^{(3)}/h$ are also parameterized, computational cost can increase highly although the imperfection approach using Eq. (6) is a simple and convenient approach. Further, accidental path switching can occur as described in the last paragraph of Section 5. In contrast, the perfection approach without imperfections can be performed using group-theoretic methods (Sattinger, 1979; Golubitsky et al., 1988; Healey ,1988). As demonstrated by Pandurangi et al. (2020), this approach has the ability to trace all the bifurcated paths regardless of the lowest and higher-order bifurcations. The analysis using the perfection approach can provide a reasonable explanation for the dependence of the second bifurcation on the imperfection magnitudes (Section 4). We believe that in the near future, the interactive understanding using the perfection and imperfection approaches is needed to accelerate the advances in the research field of complex pattern evolution caused by surface instabilities.

Finally, the present study did not focus on estimating crease nucleation as one of instabilities because the instability criterion seems to be different with Eqs. (1)–(4) (Yang et al., 2021). However, when cortical folding in mammalian brains is analyzed, it is important to investigate the interactions of wrinkling and creasing (Tallinen et al., 2014; Campos et al., 2021). In this case, the finite element meshes must be considerably finer and a smaller value of the Young's modulus ratio ($E_f/E_s \approx 1$) may be assumed. An exciting and challenging future research direction would be to trace the bifurcated paths considering the instability criteria of both wrinkling and creasing.

Declaration of Competing Interest

The authors declare that they have no known competing financial interests or personal relationships that could have appeared to influence the work reported in this paper.

CRediT authorship contribution statement

Shotaro Kikuchi: Investigation, Writing – review & editing. **Seishiro Matsubara:** Writing – review & editing. **So Nagashima:** Writing – review & editing. **Dai Okumura:** Conceptualization, Writing – original draft.

Acknowledgments

This work was partially supported by the Japan Society for the Promotion of Science (JSPS) under a Grant-in-Aid for Scientific Research (A) (JP19H00739). We thank Edanz (https://jp.edanz.com/ac) for editing a draft of this manuscript.

Appendix A. Detection of the critical values of L_{2c}/h

The critical values at the first bifurcation point on the primary path from finite element analysis of the 1×1 unit cell are shown in Fig. A.1. As shown in Fig. A.1a, when the specific values of E_f/E_s are considered in each analysis, the hexagonal or square dimple mode occurs at the critical value of L_{2c}/h, which is detected by a bisection method using the discretized values of L_2/h in the case of $L_2/L_1=\sqrt{3}$. Thus, the critical

value of L_{2c}/h in the case of $L_2/L_1=1$ is obtained by reducing them for $L_2/L_1=\sqrt{3}$. Thus, the dimensions of the unit cells are fixed depending on the value of E_f/E_s.

As shown in Fig. A.1c,b, the critical stress and wavelength are in good agreement with the theoretical values, $\sigma_{th}/E_f=(1/3)(3E_s/E_f)^{2/3}$ and $\lambda_{th}/h=2\pi(E_f/3E_s)^{1/3}$ (Allen, 1969). Note that these theoretical values are derived assuming that the thickness of the substrate is infinite (i.e., $H/h\to\infty$) and the Poisson's ratios of the film and substrate are 0.5 (i.e., incompressible). In contrast, the present study uses isotropic thermal expansion to cause compressive stress in the film so that the thickness of the film at the first bifurcation is estimated to be $h^*=(1+\alpha T_1)^3 h$, where T_1 is the critical temperature for the first bifurcation. Thus, the critical values of $\sigma_0^c(T_1)$ and λ_c/h are reduced using h^* (e.g., DuPont et al., 2010),

$$\sigma_0^{c*}/E_f=(1+\alpha T_1)^{-3}\sigma_0^c(T_1)/E_f, \tag{A.1}$$

$$\lambda_c/h^*=(1+\alpha T_1)^{-3}\lambda_c/h. \tag{A.2}$$

Eq. (A.1) simply expresses the transformation from the nominal stress to the true stress because the cross-sectional area of the film at the first bifurcation is estimated to be $A^*=(1+\alpha T_1)^3 A$, where A is the nominal value. The use of Eqs. (A.1) and (A.2) is needed to verify the results obtained from 3D finite element analysis.

Fig. A.2 shows the hexagonal and square dimple modes, $\phi_{HEX}^{(1)}$ and $\phi_{SQU}^{(1)}$, which are obtained by superposing the sinusoidal wrinkle modes in the three and two symmetric directions (Fig. 1), respectively. The hexagonal and square dimple modes occur with $k^{(1)}=6$ and 4 (i.e., they are sextuple and quadruple bifurcations), respectively, because the sinusoidal wrinkle modes in the individual directions have arbitrary phase shifts (Miyoshi et al., 2021). Both of the modes shown in Fig. A.2 are uniquely obtained by controlling the individual phase shifts to assign one dimple at the center of the unit cell. In the same way, 2×2 unit cell analysis obtains the hexagonal and square dimple modes (Fig. 6b,d).

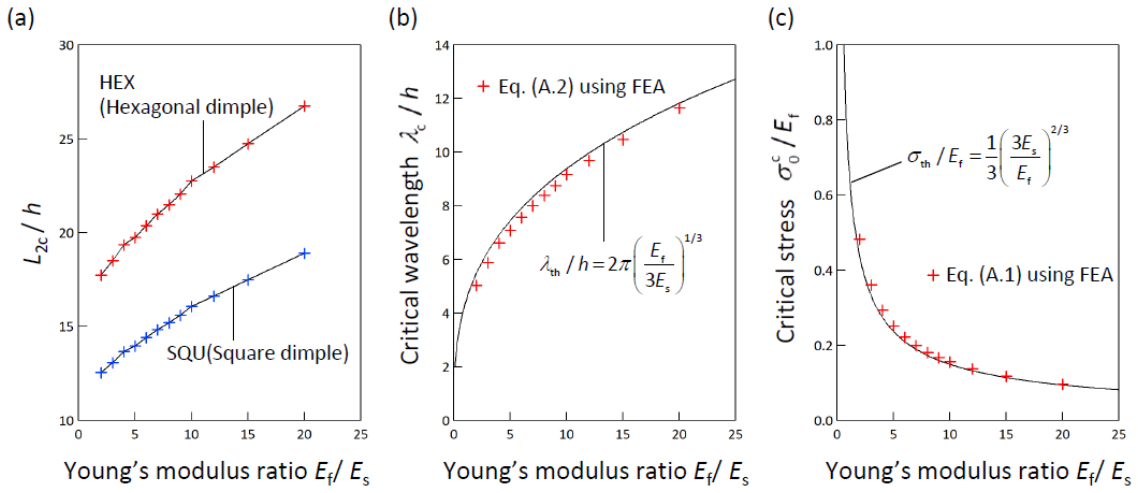

Fig. A.1. Critical values at the first bifurcation as a function of the Young's modulus ratio, E_f/E_s. (a) Critical value of L_{2c}/h for the hexagonal and square dimple modes (i.e., for $L_2/L_1=\sqrt{3}$ and =1) and comparison of the (b) critical wavelength and (c) critical stress with the theoretical values. The figures show that the critical wavelength and stress obtained using Eqs. (A.1) and (A.2) are in good agreement with the theoretical values.

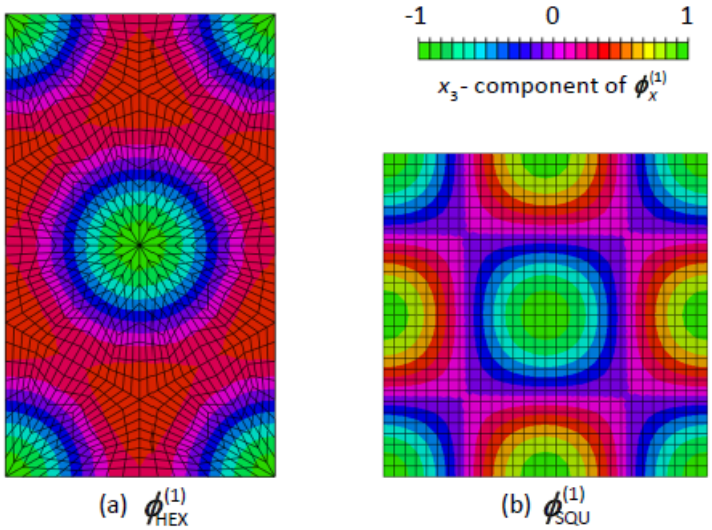

Fig. A.2. Dominant bifurcation modes at the first bifurcation obtained by analyzing the 1×1 unit cell. (a) Hexagonal dimple mode $\phi_{HEX}^{(1)}$ and (b) square dimple mode $\phi_{SQU}^{(1)}$. Although the multiplicity of the bifurcations for $\phi_{HEX}^{(1)}$ and $\phi_{SQU}^{(1)}$ is $k^{(1)}=6$ and 4, respectively, these dimple modes are uniquely obtained by controlling the individual phase shifts of the sinusoidal wrinkle modes to assign one dimple at the center of the unit cell (Miyoshi et al., 2021).

Appendix B. Potential modes in Field HA predicted from the 4×4 unit cell

When the symmetry of the hexagonal dimple pattern is considered, Field HA should

have the same modes in the three symmetric directions (Fig. 1a). Because the 2×2 unit cell produces the rectangular checkerboard mode ($\boldsymbol{\phi}^{(2)}_{\mathrm{HA0a,b}}$) with a phase shift in the x_2 direction ($k^{(2)}$=2) (Fig. 8a,b), a larger periodic unit cell (in this case, the 4×4 unit cell) is needed to obtain the identical modes ($\boldsymbol{\phi}^{(2)}_{\mathrm{HA60a,b}}$ and $\boldsymbol{\phi}^{(2)}_{\mathrm{HA60*a,b}}$) in the other two directions, i.e., $k^{(2)}$=6 using the 4×4 unit cell. Fig. B.1 shows $\boldsymbol{\phi}^{(2)}_{\mathrm{HA0a,b}}$, $\boldsymbol{\phi}^{(2)}_{\mathrm{HA60a,b}}$ and $\boldsymbol{\phi}^{(2)}_{\mathrm{HA60*a,b}}$, respectively. These figures were obtained by analyzing $\boldsymbol{\phi}^{(2)}_{\mathrm{HA0a,b}}$ (Fig. 8a,b) using a Fourier transformation. The 4×4 unit cell was not directly analyzed in Abaqus to avoid high computational cost.

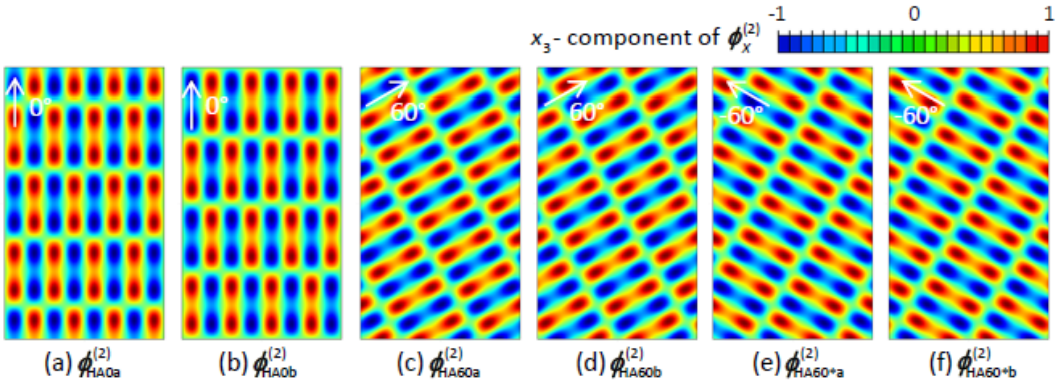

Fig. B.1. Basic bifurcation modes at the second bifurcation point in Field HA analyzed by the 4×4 unit cell. (a) $\boldsymbol{\phi}^{(2)}_{\mathrm{HA0a}}$, (b) $\boldsymbol{\phi}^{(2)}_{\mathrm{HA0b}}$, (c) $\boldsymbol{\phi}^{(2)}_{\mathrm{HA60a}}$, (d) $\boldsymbol{\phi}^{(2)}_{\mathrm{HA60b}}$, (e) $\boldsymbol{\phi}^{(2)}_{\mathrm{HA60*a}}$, and (f) $\boldsymbol{\phi}^{(2)}_{\mathrm{HA60*b}}$. The 4×4 unit cell is needed to obtain $\boldsymbol{\phi}^{(2)}_{\mathrm{HA60a,b,60*a,b}}$, i.e., $k^{(2)}$=6 for Field HA although 2×2 unit cell analysis predicts $k^{(2)}$=2. The same rectangular checkerboard mode occurs in the three symmetric directions with the phase shifts caused by the translational symmetry in the individual directions.

When the cognate modes in Field HA ($k^{(2)}$=6) are analyzed by investigating the combination of $c_1\boldsymbol{\phi}^{(2)}_{\mathrm{HA0a}}+c_2\boldsymbol{\phi}^{(2)}_{\mathrm{HA0b}}+c_3\boldsymbol{\phi}^{(2)}_{\mathrm{HA60a}}+c_4\boldsymbol{\phi}^{(2)}_{\mathrm{HA60b}}+c_5\boldsymbol{\phi}^{(2)}_{\mathrm{HA60*a}}+c_6\boldsymbol{\phi}^{(2)}_{\mathrm{HA60*b}}$ as c_i=(−1 or 0 or 1), a large number of cognate modes are expected because the total number of combinations is 3^6=729. The categorization seems to generate 11 different modes, including Modes HA(I and I+), but this investigation is already out of the scope of the present study, so the typical modes defined as Modes HA(I, I+, II, II+, III, III+, and X) are shown here to support the diversity of the bifurcations and deformations occurring on the surface of the films bonded to substrates. Modes HA(I, I+, II, II+, III, and III+) are obtained by analogizing the case of Modes SA(I, I+, II, and II+), which are described as $\boldsymbol{\phi}^{(2)}_{\mathrm{HAI}}=\boldsymbol{\phi}^{(2)}_{\mathrm{HA0a}}$ (Fig. 8a), $\boldsymbol{\phi}^{(2)}_{\mathrm{HAI+}}=\boldsymbol{\phi}^{(2)}_{\mathrm{HA0a}}+\boldsymbol{\phi}^{(2)}_{\mathrm{HA0b}}$ (Fig. 12a), $\boldsymbol{\phi}^{(2)}_{\mathrm{HAII}}=\boldsymbol{\phi}^{(2)}_{\mathrm{HA60a}}+\boldsymbol{\phi}^{(2)}_{\mathrm{HA60*a}}$

(Fig. B.2a), $\phi^{(2)}_{\mathrm{HAII+}} = \phi^{(2)}_{\mathrm{HA60a}} + \phi^{(2)}_{\mathrm{HA60b}} + \phi^{(2)}_{\mathrm{HA60*a}} + \phi^{(2)}_{\mathrm{HA60*b}}$ (Fig. B.2b), $\phi^{(2)}_{\mathrm{HAIII}} = \phi^{(2)}_{\mathrm{HA0a}} + \phi^{(2)}_{\mathrm{HA60a}} + \phi^{(2)}_{\mathrm{HA60*a}}$ (Fig. B.2c), and $\phi^{(2)}_{\mathrm{HAIII+}} = \phi^{(2)}_{\mathrm{HA0a}} + \phi^{(2)}_{\mathrm{HA0b}} + \phi^{(2)}_{\mathrm{HA60a}} + \phi^{(2)}_{\mathrm{HA60b}} + \phi^{(2)}_{\mathrm{HA60*a}} + \phi^{(2)}_{\mathrm{HA60*b}}$ (Fig. B.2d). Further, Mode HAX is described as $\phi^{(2)}_{\mathrm{HAX}} = \phi^{(2)}_{\mathrm{HA0a}} + \phi^{(2)}_{\mathrm{HA60a}} + \phi^{(2)}_{\mathrm{HA60*b}}$ (Fig. B.2e).

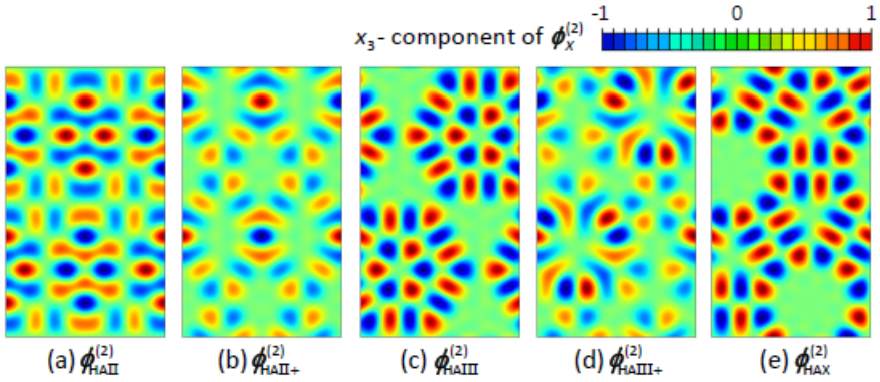

Fig. B.2. Cognate bifurcation modes at the second bifurcation point in Field HA analyzed by the 4×4 unit cell. (a) Mode HAII (e.g., $\phi^{(2)}_{\mathrm{HAII}} = \phi^{(2)}_{\mathrm{HA60a}} + \phi^{(2)}_{\mathrm{HA60*a}}$), (b) Mode HAII+ (e.g., $\phi^{(2)}_{\mathrm{HAII+}} = \phi^{(2)}_{\mathrm{HA60a}} + \phi^{(2)}_{\mathrm{HA60b}} + \phi^{(2)}_{\mathrm{HA60*a}} + \phi^{(2)}_{\mathrm{HA60*b}}$), (c) Mode HAIII (e.g., $\phi^{(2)}_{\mathrm{HAIII}} = \phi^{(2)}_{\mathrm{HA0a}} + \phi^{(2)}_{\mathrm{HA60a}} + \phi^{(2)}_{\mathrm{HA60*a}}$), (d) Mode HAIII+ (e.g., $\phi^{(2)}_{\mathrm{HAIII+}} = \phi^{(2)}_{\mathrm{HA0a}} + \phi^{(2)}_{\mathrm{HA0b}} + \phi^{(2)}_{\mathrm{HA60a}} + \phi^{(2)}_{\mathrm{HA60b}} + \phi^{(2)}_{\mathrm{HA60*a}} + \phi^{(2)}_{\mathrm{HA60*b}}$), and (e) Mode HAX (e.g., $\phi^{(2)}_{\mathrm{HAX}} = \phi^{(2)}_{\mathrm{HA0a}} + \phi^{(2)}_{\mathrm{HA60a}} + \phi^{(2)}_{\mathrm{HA60*b}}$). Modes HA(I and I+) are expressed as $\phi^{(2)}_{\mathrm{HAI}} = \phi^{(2)}_{\mathrm{HA0a}}$ (Fig. 8a) and $\phi^{(2)}_{\mathrm{HAI+}} = \phi^{(2)}_{\mathrm{HA0a}} + \phi^{(2)}_{\mathrm{HA0b}}$ (Fig. 12a). Note that these are the typical cognate modes obtained by analogizing the case of Modes SA(I, I+, II, and II+) so Mode HAX is recognized as a higher mode similar to Modes SA(III and IV).

Although Modes HA(II, II+, III, III+, and X) are simply obtained by Fourier transformation (not Abaqus), the imperfections (Fig. B.3) obtained by superposition of the first and second bifurcation modes (Figs. 1a and B.2) are useful to determine the deformations on the bifurcated path, as discussed in Sections 5 and 6. The resulting deformation patterns seem to be unique patterns, and Modes HA(II, II+, III, and III+) (Fig. B.3a–d) are expected to trigger evolution of periodical labyrinth or disordered herringbone patterns, whereas Mode HAX (Fig. B.3e) looks like a satellite image of a typhoon (a typhoon pattern seems to be produced by the periodic arrangement of the grooves formed by coalescence of selected dimples). Although the 4×4 unit cell (the 2×2 unit cell was used in the present study) requires high computational cost in finite element analysis, the present study successfully provides the imperfections consisting of the first and second bifurcation modes in Field HA. This indicates that because the potential imperfections are already prepared, an analytical approach (e.g., an analytical

upper bound method, Cai et al., 2011) may be able to estimate the energy difference among the corresponding deformation patterns.

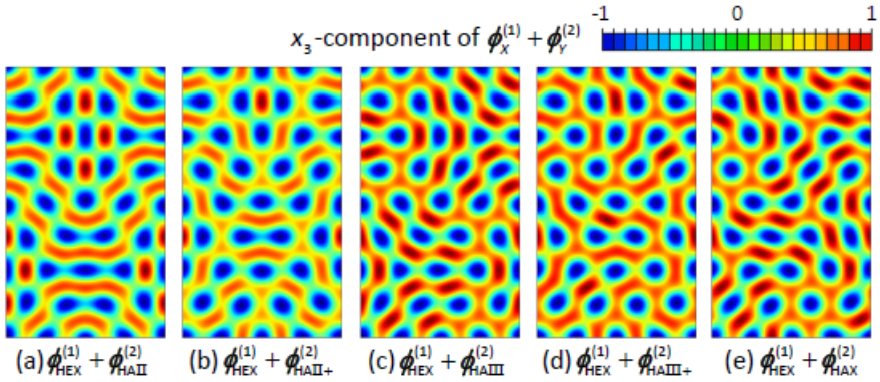

Fig. B.3. Initial imperfections generated by Modes HA(II, II+, III, III+, and X). (a) $\phi_{HEX}^{(1)} + \phi_{HAII}^{(2)}$, (b) $\phi_{HEX}^{(1)} + \phi_{HAII+}^{(2)}$, (c) $\phi_{HEX}^{(1)} + \phi_{HAIII}^{(2)}$, (d) $\phi_{HEX}^{(1)} + \phi_{HAIII+}^{(2)}$, and (e) $\phi_{HEX}^{(1)} + \phi_{HAX}^{(2)}$. Although postbuckling analysis was not performed in the present study, these imperfections are expected to trigger evolution of periodical labyrinth or disordered herringbone patterns.

References

Abaqus 6.14 User Documentation, 2014. Dassault Systems SIMULIA Corporation.

Allen, H.G., 1969. In: Analysis and design of sandwich panels. Pergamon Press, New York.

Audoly, B., Boudaoud, A., 2008a. Buckling of a thin film bound to a compliant substrate—Part I: formulation, linear stability of cylindrical patterns, secondary bifurcations. J. Mech. Phys. Solids 56, 2401–2421.

Audoly, B., Boudaoud, A., 2008b. Buckling of a thin film bound to a compliant substrate—Part II: A global scenario for the formation of herringbone pattern. J. Mech. Phys. Solids 56, 2422–2443.

Audoly, B., Boudaoud, A., 2008c. Buckling of a thin film bound to a compliant substrate–Part III: Herringbone solutions at large buckling parameter. J. Mech. Phys. Solids 56, 2444–2458.

Bertoldi, K., Boyce, M.C., Deschanel, S., Prange, S.M., Mullin, T., 2008. Mechanics of deformation-triggered pattern transfromations and superelastic behavior in periodic elastomeric structures. J. Mech. Phys. Solids 56, 2642–2668.

Biot, M.A., 1963. Surface instability of rubber in compression. Appl. Sci. Res., Sec. A 12, 168–182.

Biot, M.A., 1965. Mechanics of incremental deformations: theory of elasticity and viscoelasticity of initially stressed solids and fluids, including thermodynamic foundations and applications to finite strain, Wiley.

Breid, D., Crosby, A.J., 2009. Surface wrinkling behavior of finite circular plates. Soft Matter 5, 425–431.

Breid, D., Crosby, A.J., 2011. Effect of stress state on wrinkle morphology. Soft Matter 7, 4490–4496.

Budday, S., Steinmann, P., Kuhl, E.. 2014. The role of mechanics during brain development. J. Mech. Phys. Solids 72, 75–92.

Cai, S., Breid, D., Crosby, A.J., Suo, Z., Hutchinson, J.W., 2011. Periodic patterns and energy states of buckled films on compliant substrates. J. Mech. Phys. Solids 59, 1094–1114.

Campos, L.da.C., Hornung, R., Gompper, G., Elgeti, J., Caspers, S., 2021. The role of thickness inhomogeneities in hierarchical cortical folding, Neuro Image 231, 117779.

Chen, X., Hutchinson, J.W., 2004. Herringbone buckling patterns of compressed thin films on compliant substrates. J. Appl. Mech. 71, 597–603.

Combescure, C., Elliott, R.S., Triantafyllidis, N., 2020. Deformation patterns and their stability in finitely strained circular cell honeycombs. J. Mech. Phys. Solids 142, 103976.

DuPont Jr, S.J., Cates, R.S., Stroot, P.G., Toomey, R., 2010. Swelling-induced instabilities in microscale, surface-confined poly(N-isopropylacryamide) hydrogels. Soft Matter 6, 3876–3882.

Gent, A.N., Cho, I.S., 1999. Surface instabilities in compressed or bent rubber blocks. Rubber Chem. Technol. 72, 253–262.

Geymonat, G., Müller, S., Triantafyllidis, N., 1993. Homogenization of nonlinearly elastic materials, microscopic bifurcation and macroscopic loss of rank-one convexity. Arch. Ration. Mech. Anal. 122, 231–290.

Gibson, L.J., Ashby, M.F., 1997. Cellular Solids: Structure and Properties, 2nd Edition. Cambridge University Press, Cambridge.

Golubitsky, M., Stewart, I., Schaeffer, D.G., 1988. Singularities and Groups in Bifurcation Theory, Volume II. Springer, New York.

Goriely, A., 2016. The mathematics and mechanics of biological growth. Springer.

Guvendiren, M., Yang, S., Burdick, J.A., 2009. Swelling-Induced surface patterns in hydrogels with gradient crosslinking density. Adv. Funct. Mater. 19, 3038– 3045.

Healey, T.J., 1988. A group-theoretic approach to computational bifurcation problems with symmetry. Comput. Meth. Appl. Mech. Eng. 67, 257–295.

Healey, T.J., 1989. Why bifurcation: a study of a reticulated dome. In Ang. A.H.-S. editor. Structural Design, Analysis and Testing, 942–948.

Hill, R., 1958. A general theory of uniqueness and stability in elastic–plastic solids. J. Mech. Phys. Solids 6, 236–249.

Hong, W., Liu, Z., Suo, Z., 2009. Inhomogeneous swelling of a gel in equilibrium with a solvent and mechanical load. Int. J. Solids Struct. 46, 3282–3289.

Huang, Z.Y., Hong, W., Suo, Z., 2005. Nonlinear analyses of wrinkles in a film bonded to a compliant substrate. J. Mech. Phys. Solids 53, 2101–2118.

Kang, M.K., Huang, R., 2010a. A variational approach and finite element implementation for swelling of polymeric hydrogels under geometric constraints. J. Appl. Mech. 77, 061004.

Kang, M.K., Huang, R., 2010b. Swelling-induced surface instability of confined hydrogel layers on substrates. J. Mech. Phys. Solids 58, 1582–1598.

Kuhl, E., 2016. Unfolding the brain. Nature Phys. 12, 533–534.

Miyoshi, H., Matsubara, S., Okumura, D., 2021. Bifurcation and deformation during the evolution of periodic patterns on a gel film bonded to a soft substrate. J. Mech. Phys. Solids 148, 104272.

Ohno, N., Okumura. D., Noguchi, H., 2002. Microscopic symmetric bifurcation condition of cellular solids based on a homogenization theory of finite deformation. J. Mech. Phys. Solids 50, 1125–1153.

Ohno, N., Okumura, D., Niikawa, T., 2004. Long-wave buckling of elastic square honeycombs subject to in-plane biaxial compression. Int. J. Mech. Sci. 46, 1697–1713.

Okumura, D., Inagaki, T., Ohno, N., 2015. Effect of prestrains on swelling-induced buckling patterns in gel films with a square lattice of holes. Int. J. Solids Struct. 58, 288–300.

Okumura, D., Ohno, N., Noguchi, H., 2002. Post-buckling analysis of elastic honeycombs subjected to in-plane biaxial compression. Int. J. Solids Strut. 39, 3487–3503.

Okumura, D., Ohno, N., Noguchi, H., 2004. Elastoplastic microscopic bifurcation and post-bifurcation behavior of periodic cellular solids. J. Mech. Phys. Solids 52, 641–666.

Okumura, D., Sugiura, J., Tanaka, H., Shibutani, Y., 2018. Buckling and postbuckling of etching-induced wiggling in a bilayer structure with intrinsic compressive stress. Int. J. Mech. Sci. 141, 78–88.

Pandurangi, S.S., Elliott, R.S., Healey, T.J., Triantafyllidis, N., 2020. Stable spatially localized configurations in a simple structure – a global symmetric-breaking approach. J. Elast. 142, 163–199.

Papka, S.D., Kyriakides, S., 1999. Biaxial crushing of honeycombs—Part I: experiments. Int. J. Solids Struct. 36, 4367–4396.

Richman, D.P., Stewart, R.M., Hutchinson, J.W., Caviness, V.S.Jr., 1975. Mechanical model of brain convolutional development. Science 189, 18–21.

Sattinger, D.H., 1979. Group theoretic methods in bifurcation theory. Springer, Germany.

Tallinen, T., Chung, J.Y., Biggins, J.S., Mahadevan, L., 2014. Gyrification from constrained cortical expansion. PNAS USA 111, 12667–12672.

Tallinen, T., Chung, J.Y., Rousseau, F., Girard, N., Lefèvre, J., Mahadevan, L., 2016. On the growth and form of cortical convolutions. Nature Physics 12, 588–593. .

Tallinen, T., Biggins, J.S., 2015. Mechanics of invagination and folding: hybridized instabilities when one soft tissue grows on another. Phys. Rev. E 92, 022720.

Yang, P., Fang, Y., Yuan, Y., Meng, S., Nan, Z., Xu, H., Imtiaz, H., Liu, B., Gao, H., 2021. A perturbation force based approach to creasing instability in soft materials under general loading conditions. J. Mech. Phys. Solids 151, 104401.